DEPARTMENT OF PHYSICS

TECHNISCHE UNIVERSITÄT MÜNCHEN

Bachelor's Thesis

Analysis of the Λ^0-Ξ^- Correlations with ALICE at the LHC

Analyse der Λ^0-Ξ^- Korrelationen mit ALICE am LHC

Autor:	Georgios Mantzaridis
Betreuer:	Dr. Otón Vázquez Doce
Erstprüferin (Themenstellerin):	Prof. Dr. L. Fabbietti
Zweitprüfer:	Prof. Dr. H. Kroha
Submission Date:	05.10.2020

Abstract

This work demonstrates an algorithm to perform a correlation analysis on Λ-Ξ^- paris the femtoscopy method, which can also be extended to other hyperon-hyperon pairs with. Its efficiency in dealing with possible auto-correlations is demonstrated with Pythia simulations and subsequently a first analysis is performed on Λ-Ξ^- correlations using data from high multiplicity proton-proton collisions at $\sqrt{s} = 13\text{TeV}$ from the ALICE experiment at CERN. The result is compared with theoretical predictions for the Λ-Ξ^- interaction. The statistical uncertainties are large because of the lower yield of particles containing strange quarks compared to those containing up and down quarks. Nevertheless, the result is not able to reproduce the calculations from leading order chiral effective field theory (LO EFT) and thus hinting to a weaker interaction than anticipated in these calculations.

Kurzfassung

In der vorliegenden Arbeit wird ein Algorithmus presentiert, um Korrelationsanalysen von Λ-Ξ^- Paaren mit der Femtoscopy Methode durchzuführen, die auch auf andere Hyperon-Hyperon Paare ausgeweitet werden kann. Die Effizienz des Algorithmus beim Umgang mit Autokorrelationen wird mithilfe von Pythia Simulationen demonstriert. Im Anschluss wird eine erste Analyse der Λ-Ξ^- Paare durchgeführt. Die Daten stammen von Proton- Proton Kollisionen mit hoher Multiplizität und bei Schwerpunkgsenergien von $\sqrt{s} = 13\,\text{TeV}$, die am ALICE Experiment am CERN aufgenommen wurden. Das Ergebnis wird mit theoretischen Vorhersagen für die Λ-Ξ^- Wechselwirkung verglichen. Die statistischen Unsicherheiten sind hoch, weil die Produktion von Teilchen mit strange Quarks geringer sind, als für die mit den beiden leichteren up und down Quarks. Trotzdem ist das Ergebnis nicht in der Lage die Berechnungen von LO EFT zu reproduzieren, was auf eine schächere Wechselwirkung hindeutet, als in diesen Berechnungen angenommen wird.

Contents

1 Introduction

The hyperon puzzle in neutron stars

Neutron stars are the remnants of heavy stars with masses above 8 solar masses. When the core of such a star collapses, the outer shells are expelled into the universe in a Supernova. Behind remain the most dense objects directly observable with densities surpassing those of regular nuclear matter. The heaviest observed neutron stars reach up to two solar masses and have radii of the order of 10km (about a factor of 10^5 less then the radius of the sun) [1]. They offer a great opportunity to study and test theories under extreme conditions and in particular under extremely large densities. While experiments at the LHC or RHIC probe into the high temperature part of the phase diagram of high density nuclear matter (temperatures around 150 MeV) using relativistic heavy ion collisions, neutron stars are located at the low temperature regime of it (with temperatures around 1MeV [2]).

The microscopic description of neutron stars is given by the equation of state (EoS) for dense matter, which relates the pressure to the density in a neutron star. This description of the EoS depends on parameters that characterize the interaction and behaviour of the particles involved in a neutrons star. It is directly translatable into a mass-radius relation and it is the topic of current research to determine accurately the composition of neutron stars. The exact form of the EoS is still not known [3]. However, there are different models which predict different mass-radius relations, as shown in figure 1.1. The left panel shows different predictions for the density of states and the right panel shows the corresponding mass radius relation [1]. Precise observations (ideally of the mass and the radius simultaneously) allow to rule out EoSs when for example a neutron star is observed, which does lies outside of the predicted mass-radius relation.

The densities inside a neutron star are large enough for hyperons to be produced. Hyperons

	Valence quarks	Mass (GeV/c^2)
Λ	u d s	1.116
Σ^+	u u s	1.189
Σ^0	u d s	1.193
Σ^-	d d s	1.197
Ξ^0	u s s	1.315
Ξ^-	d s s	1.322
Ω^-	s s s	1.672

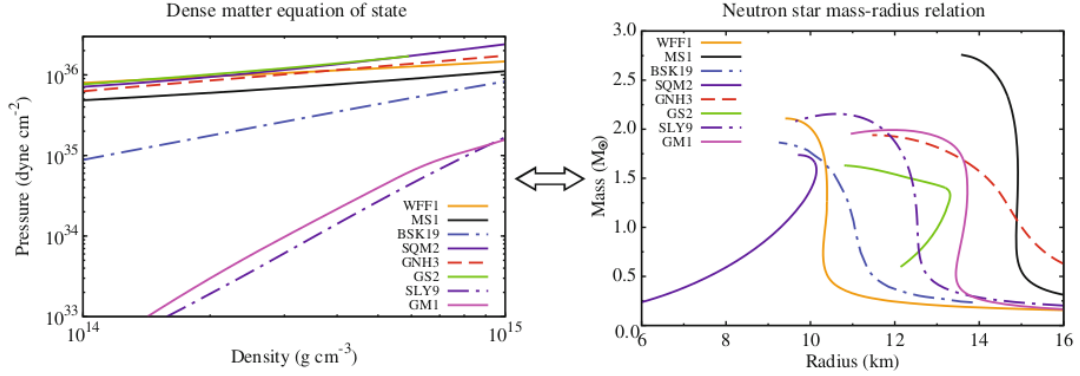Table 1.1: Overview of the hyperons (without their antiparticles) [4]

Figure 1.1: Different EoS and their mapping to mass-radius relations [1]

are baryons with at least one strange quark. A short overview is given in table 1.1. Under earth like circumstances hyperons have a very small lifetime. But the extreme conditions inside the neutron star would make it even energetically preferable for nucleons to get conveyed into hyperons and exist stably. This would lower the fermi pressure since new degrees of freedom are added and make the EoS softer, which in turn would lower the possible maximum mass of stable neutron stars. Although there exist some models, which consider hyperons and allow a maximum mass of $2M_\odot$, the general consensus has settled to a value between 1.4 and 1.8 $M_\odot$ [5]. The measurement of massive neutron stars like the pulsar J1614-2230 in 2010 ($1.97 \pm 0.04 M_\odot$)[6] and J0348+0432 in 2013 ($2.01 \pm 0.04 M_\odot$)[7] show that there is something missing in the understanding of neutron stars. This is the so called hyperon puzzle. A possible solution to this could be repulsive hyperon- hyperon (YY) and hyperon- nucleon (YN) interactions, since they would stiffen the EoS and thus bring the existence of exotic matter in massive neutron stars in accordance to observations. The study of three body interactions with hyperons involved such as p-p-Λ^0 could also help to solve this puzzle.

Experimental data on these interaction is very scarce, since hyperons have too small lifetimes to perform hyperon- hyperon collision experiments and only very little data exists on hyperon- nucleon collisions. The femtoscopy method, which will be the central topic of the next chapter, is an alternative method to extract the interaction potentials out of proton proton and heavy nuclei collisions. Various studies have been performed so far, among them the YN interaction p-Ω^- and p-Ξ^- [8], p-Λ and the YY interaction Λ-Λ [9].

Why Λ-Ξ^-?

In the same spirit, this thesis will focus on the analysis of the YY Λ-Ξ^- interaction. Apart from being an YY interaction worth studying (so far only Λ-Λ^0 was approached), the form of the correlation function would have direct implications on the interpretation of the already

measured p-Ω^- interaction. The comparison with first principle calculations with lattice QCD did not match up, because the latter underestimated the data. These calculations do not consider so called strangeness rearrangement processes $p\Omega^- \to \Lambda\Xi^-, \Sigma^0\Xi^-$ [8]. The strength of these coupled channels is not known, since there exists no experimental information on that. The analysis of the Λ^0-Ξ^- interaction could thus provide also an important ingredient for the p-Ω interaction by reducing a large uncertainty in its comparison with theoretical calculations.

The aim is to develop a reliable algorithm for the analysis of the Λ-Ξ^- interaction. For that, a method will be presented in chapter 4, which is able to select the correct particle candidates when they have been ambiguously reconstructed along with fake candidates. Further, a pair cleaning method is implemented which blocks auto-correlated pairs and still allows for a good estimation of the remaining feed-down contributions. The robustness of this algorithm will be demonstrated with Monte Carlo simulations. This demonstration will be concluded with a first comparison of experimental data to various theoretical predictions for the Λ-Ξ^- interaction. Before that, the femtoscopy method will be described in chapter 2 followed by chapter 3, a short introduction to the ALICE experiment at the LHC, which provided the data for this analysis. Finally, chapter 5 provides a summary and an outlook to future work on this topic.

2 The femtoscopy method

As discussed, relativistic heavy ion collisions and neutron stars are complementary sources for studying dense nuclear matter. The femtoscopy method can be applied in the former. It originates from the work of Hanbury Brown and Twiss, where the aim was to determine light emitting source sizes (dominantly stellar objects) by measuring correlated photon pairs [10]. This method was also applied in proton-antiproton collisions by measuring the correlation of emitted pion pairs, and made the transition to correlations of non identical particles and was established as a high precision measuring method under its current name in relativistic heavy ion collisions. These collisions create dense and high temperature hadronic matter, which is impossible to study directly due to the small size ($\sim 10^{-14}$m) and lifetime ($\sim 10^{-22}$s) of this system. After cooling down and reaching the freeze out temperature the system emits hadrons and can thus be regarded as a particle emitting source. In femtoscopy those hadrons are measured in order to extract information from the collision system. This can and has been expanded to other collision systems, namely proton-proton (pp) and proton-lead (pPb). The central part of this method is the two pair correlation function which is defined as

$$C\left(\vec{p_1}, \vec{p_2}\right) = \frac{P\left(\vec{p_1}, \vec{p_2}\right)}{P\left(\vec{p_1}\right) P\left(\vec{p_2}\right)} = \frac{E_1 E_2 dN / \left(d^3 p_1 d^3 p_2\right)}{\left(E_1 dN / d^3 p_1\right)\left(E_2 dN / d^3 p_2\right)}, \tag{2.1}$$

where $P\left(\vec{p_1}, \vec{p_2}\right)$ is the probability for finding a particle with momentum $\vec{p_1}$ when the second particle has been emitted with a momentum of $\vec{p_2}$, while $P\left(\vec{p_1}\right)$ and $P\left(\vec{p_2}\right)$ are the probabilities of finding a single particle with the respective momentum. The astronomical interferometry origin of the method becomes evident by replacing $P\left(\vec{p_i}\right)$ in the denominator with the photon intensity $\langle I_i \rangle$ and the nominator with $\langle I_1 I_2 \rangle$. Finally, the correlation function can be calculated by the two particle cross section divided by the product of the two single particle cross sections (all three of them being Lorentz invariant quantities) [11].

2.1 The theoretical correlation function

The correlation between two particles does not only depend on the properties of the emitting source but also on their final state interactions (FSI) (and in the case of identical particles on quantum statistics) [12]. The FSI could be due to the Coulomb repulsion or attraction or even strong force interactions. All of this is considered in the computation of the theoretical calculation, given by

$$C(k^*) = \int S(\vec{r^*}) |\psi(k^*, \vec{r^*})|^2 d^3 r, \tag{2.2}$$

where $S(\vec{r^*})$ is the source function and $\psi(k^*, \vec{r^*})$ is the pair wave function. It is expressed in the rest frame of the particle pair's center of mass, so $\vec{r^*}$ is the relative distance between the two particles and $\vec{k^*}$ the reduced relative momentum defined as

$$\vec{k^*} = \frac{m_2 \vec{p_1^*} - m_1 \vec{p_2^*}}{m_1 + m_2}, \tag{2.3}$$

where $\vec{p_i^*}$ is the momentum of particle i in the particle rest frame which is denoted by the $*$.

The source function is a spatial probability density for the emission of a pair with the relative distance $\vec{r^*}$. The pair wave function contains the interaction potential of the particle pair. Over the last decades femtoscopy was used to study the source function using hadrons with rather well known interaction such as protons and pions. It is also possible to go the other way and extract the the interaction potential out of the correlation function, when the source is known. In particular, it makes the study of YN and YY interactions possible. The source function has two contributions: The core source, where primordial particles are emitted from and a halo coming from shortly decaying resonances [13]. Their decay lengths (less then 10fm) are small enough so that the daughters can experience final state interactions and thus to be considered as primary particles, while the resonances themselves are assumed to not interact in such small time scales. By assuming Gaussian profile for the core source

$$S_G\left(\vec{r^*}\right) = \left(4\pi r_0^2\right)^{-3/2} \cdot \exp\left(-\frac{\vec{r^*}^2}{4r_0^2}\right), \tag{2.4}$$

it can be fully characterized by the core radius r_{core}, which was found to dependant of the transverse mass m_T and multiplicity [12]. The transverse mass is defined as

$$m_T = \sqrt{k_T^2 + m^2} \tag{2.5}$$

with $k_T = |\vec{p}_{T,1} + \vec{p}_{T,2}|/2$ being the pair transverse momentum and m the average mass of the pair. However, in [13] it was demonstrated that the m_T dependence of r_{core} is the same for p-p and p-Λ pairs under the assumption of a Gaussian core. For this work, it will be further assumed that the same is true for every baryon-baryon pair. The halo from shortly decaying resonances extends the effective source radius as illustrated in figure 2.1. Two primordial resonances are emitted from the source at the distance $\vec{r}_{core}$, like also two primordial particles would be. They both travel a distance $\vec{s_i^*}$ before decaying into the baryons and therefore the effective relative distance of emission is modified to $\vec{r^*}$. With EPOS simulations and applying the standard hadronization model (SHM) it is possible to calculate the modification of this halo. More details on the treatment in this analysis will be given in section 4.8.

2.2 The experimental correlation function

In order to extract the interaction potential, the correlation function needs to be obtained experimentally and then compared to the theoretically computed function. For that, the distribution of k^* (as defined in (2.3)) of correlated pairs, the so called same event distribution
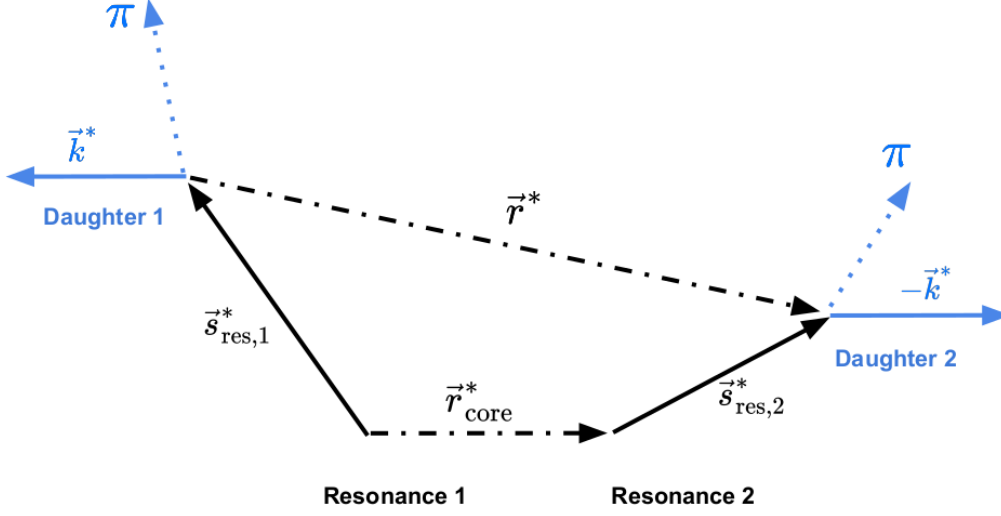
Figure 2.1: Illustration of the effect of shortly decaying resonances on the Source [13]

(SE), is divided by an uncorrelated, the so called mixed event distribution (ME). For the former, one has to pair the particles of interest which were produced in the same collision (event) while for the latter, a mixing technique is necessary to ensure that uncorrelated pairs (from different events) are paired together without introducing any biases.

$$C(k^*) = \mathcal{N} \cdot \frac{N_{same}(k^*)}{N_{mixed}(k^*)} \tag{2.6}$$

The normalization parameter $\mathcal{N}$ is introduced to ensure that the correlation function goes to 1 for large k^* (typically $> 200\text{MeV}/c$), since for large relative momenta one does not expect any correlation due to femtoscopic effects. Other effects modify the correlation in this non femtoscopic region, as will be discussed in the following. Sections 4.4 and 4.5 will elaborate more on the methods used in this analysis to obtain the SE and ME respectively.

2.3 Comparing the experimental and theoretical correlation function

2.3.1 Corrections

Before comparing the theoretical and experimental correlation functions there have to be taken corrections for experimental effects into account [14]:

- non femtoscopic background

- contamination of miss identified and feed down particles

The first affects the correlation function such that it does not approach unity for relative momenta above 300 MeV. The reason is thought to lie in energy conservation and it is included in the correlation function by adding a linear or quadratic baseline function to the theoretical models. Feed-down contributions come from decay products of other primary particles, for example a secondary Λ which comes from the decay of a Ξ^0. The primary particles propagate their correlations to their decay daughters because of their FSIs with other primaries. Thus, even thought the daughters themselves have no FSIs because their appearance is on a larger timescale (the decay time of the mother particles), they never the less contribute to the correlation function with the signal of their mothers. In the above example one would not measure the correlation of the Λ but instead that of its mother Ξ^0. Miss identified particles (or impurities) on the other hand are assumed to be uncorrelated. Their contribution is flat and thus has no influence on the shape of the correlation function. Both contributions can not be completely excluded from the analysis. It is difficult to differentiate between primary and secondary particles and there will always be a certain amount of fake particles present (for example due to combinatorial background). Instead, they have to be considered in the theoretical computation of the correlation function before the comparison. With the method of the λ parameters one can account for those two contributions, when the correlation functions of the feed-down (and impurity) pairs, denoted by the indices i and j, are known:

$$C_{\text{femto}}\left(k^*\right) = 1 + \lambda_{\text{real}} \cdot \left(C_{\text{real}}\left(k^*\right) - 1\right) + \sum_{ij} \lambda_{ij} \left(C_{ij}\left(k^*\right) - 1\right) \tag{2.7}$$

The λ parameters are calculated by

$$\lambda_{ij} = \lambda_i \cdot \lambda_j = \mathcal{P}_i f_i \cdot \mathcal{P}_j f_j \tag{2.8}$$

as shown in the Appendix of [14]. Here f is the fraction the fake candidates or of particles originating from the feed-down channel of interest and $\mathcal{P}$ the purity of the respective particles. The purity can be obtained by fitting the invariant mass spectra of the selected particles, while for the fractions one has to fit templates from Monte Carlo simulations to the data. More details on the implementation in this work will be discussed in section 4.7.

In principal also the finite momentum resolution of the detector has to be taken into account. As seen in the p-Ξ^- and Λ-Λ analysis in [9], the corrections are very small. Thus they will not be considered in this work since the statistical uncertainties will be too high to be sensitive to these effects.

2.3.2 The Lednický model

Lednický and Lyuboshitz proposed an analytical model for the calculation of the correlation function [15]. It uses the assumption of a Gaussian source (2.4) function, especially in order

to be analytically solvable. As an example, the correlation function for uncharged particles is

$$
\begin{aligned}
C\left(k^{*}\right)_{\text{Lednicky}} = 1 + \sum_{S} \rho_{S} & \left[\frac{1}{2} \left| \frac{f\left(k^{*}\right)^{S}}{r_{0}} \right|^{2} \left(1 - \frac{d_{0}^{S}}{2\sqrt{\pi}r_{0}} \right) + \frac{2\Re f\left(k^{*}\right)^{S}}{\sqrt{\pi}r_{0}} F_{1}\left(Q_{\text{inv}}\, r_{0}\right) \right. \\
& \left. - \frac{\Im f\left(k^{*}\right)^{S}}{r_{0}} F_{2}\left(Q_{\text{inv}}\, r_{0}\right) \right]
\end{aligned}
\tag{2.9}
$$

with the complex scattering amplitude, evaluated with the effective range approximation

$$
f\left(k^{*}\right)^{S} = \left(\frac{1}{f_{0}^{S}} + \frac{1}{2} d_{0}^{S} k^{*2} - i k^{*} \right)^{-1}
\tag{2.10}
$$

where S is the total spin of the particle pair, f_{0}^{S} the scattering length and d_{0}^{S} the effective range. In ρ_{S} the pair fraction emitted into the spin state S is contained. By convention an attractive interaction leads to a positive scattering length [14]. In equation (2.9) $F_{1}(Q_{inv}r_{0})$ and $F_{2}(Q_{inv}r_{0})$ are analytical functions which originate from the Gaussian source approximation (2.4).

2.3.3 The CATS framework

The "**C**orrelation **A**nalysis **T**ool using the **S**chrödinger equation" framework offers a numerical way for calculating the correlation function. It has the Lednický model is implemented but is further than that able to take any functional form for the interaction potential as an input. Further, it has a variety of tuned potentials for different YN interactions already implemented and provides the ability to define new ones. It enables the user to define also other source functions besides that of a Gaussian distribution. After defining a interaction potential and a soucre function, CATS solves the Schrodinger Equation and computes the correlation function, which can then be used to fit the experimentally obtained function [16].

3 Experimental setup

3.1 The LHC

Constructed inside the tunnel of the former LEP (**L**arge **E**lecton **P**ositron collider) the **L**arge **H**adron **C**ollider is a circular hadron accelerator with a circumference of 26.7km. It is run by the European Organization for Nuclear Research (CERN) and hosts the four experiments ALTAS, CMS, ALICE and LHCb. As a particle particle accelerator, it needs two distinct acceleration rings, which are brought to collision at four crosspoints, where the experiments are located. Besides being the largest particle collider with the largest collision energies in the world, which is a key achievement in itself, it hosted the experimental detection of the Higgs Boson in 2012. Thus it delivered the last missing particle to complete the standart model of particle physics. [17]

Currently (August 2020) the LHC is in its second Long Shutdown period (LS2) until the spring of 2021 after it had been in the Run 2 phase for four years between 2015 and 2018 [18]. During Run 2, the LHC ran most of the time in the proton proton mode with beam energies of 6.5 TeV for each beam [19]. However, a few weeks were dedicated also to Pb-Pb collisions (with beam energies $E_b = 6.37$ TeV $\cdot Z$) and p-Pb collisions (with $E_b = 4$TeV for protons and $E_b = 6.5$TeV for Pb) [20]. The analysis in this thesis focuses on the data acquired from pp collisions during Run 2, meaning a center of mass energy of $\sqrt{s_{pp}} = 13$TeV.

3.2 The ALICE Experiment

The ALICE Experiment (acronym for **A** **L**arge **I**on **C**olliding **E**xperiment) was designed to study the dense matter created by relativistic heavy ion collisions. Its excellent particle identification and reconstruction as well as the collision energies, which provide the necessary phase space for strange quarks to be created, make it a perfect experimental environment to apply the femtoscopy method. Since only hadrons are the particles of interest, only the main three detector components responsible for their reconstruction and identification will be summarized in the following. An overview of the complete ALICE setup with links to further information can be found here [21]

3.2.1 Inner Tracking System (ITS)

The **I**nner **T**racking **S**ystem is the first part of the detector. It is made up of six cylindrical layers, which are depicted in figure 3.1. The two most inner ones are silicon pixel detectors (SPDs). Their high resolution is necessary, since the number of particles per cm exceeds 50
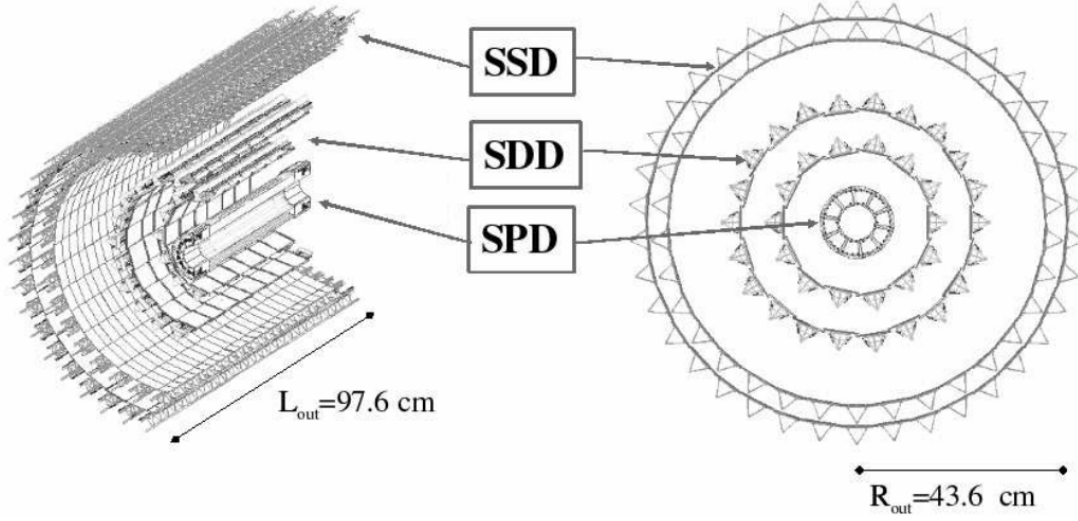
Figure 3.1: The ITS with its three layers [22]

in this region. The SPDs are responsible for the localization of the primary vertex, which they can do with a precision better than 100μm. They reconstruct slso the secondary vertices, meaning the vertices of weak decays such as these of Λs and Ξs as well as those of D and B mesons. The next two layers are silicon drift detectors (SDDs) which offer dE/dx information for particle identification. Following them, the last four layers are silicon strip detectors (SSDs). They have an analogous readout with a dynamic range large enough that they are used for particle identification of particles with low transverse momentum ($p_T < 200\text{GeV/c}$). The identification of charged particles is performed by measuring the energy loss per traveld distance, which depends of the particles mass, according to the Bethe- Bloch formular [23]:

$$-\frac{\mathrm{d}E}{\mathrm{d}x} = \frac{4\pi n z^2}{m_e c^2 \beta} \left(\frac{e^2}{4\pi\epsilon_0}\right)^2 \left[\ln\left(\frac{2m_e c^2 \beta^2}{I\cdot(1-\beta^2)}\right) - \beta^2\right] \tag{3.1}$$

Particles with a transverse momentum just large enough to be reconstructed at all, are reconstructed there. Further, the SSDs are essential for matching the tracks of the ITS to those of the TPC, the next part of the detector. [22]

3.2.2 Time Projection Chamber (TPC)

The **T**ime **P**rojection **C**hamber is the main detector compontent for particle identification. It is the cylinder around the ITS with an inner radius of 85cm and an outer radius of 250cm filled with the counting gas mixture $\mathbf{Ne - CO_2 - N_2}$ at atmospheric pressure. With a length of 500cm its total gas volume is 90m^3 . Thus it covers the whole 2π azimuthal angle and the pseudorapidity range $-0.9 < \eta < 0.9$. Particles are identified via their energy loss in the gas volume according to the Bethe- Bloch formular (3.1). The charge is determined by
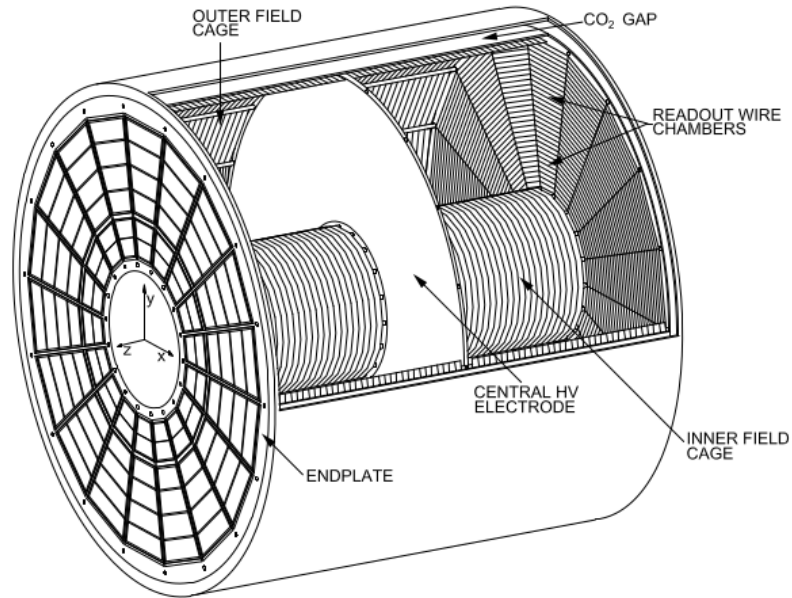
Figure 3.2: A sketch of the ALICE TPC [24]

the particles curvature in the magnetic field (0.5T) inside the TPC, produced by a solenoid. While traversing through the TPC, the particles ionize the gas and the now free electrons drift towards the endplates of the TPC, where they are measured in one of the 648 readout chambers, divided into 18 sections (per endplate). Together with timing information the point of ionization can be precisely calculated and from that the particles trajectory. The drifting is made possible due to the uniform electric field created by the field cage, which at the same time provides the mechanical structure as well as containment of the gas while offering the minimal radiation length possible. The central electrode operates under a voltage of 100kV thus providing a high electron drift velocity. In the outer part of the TPC cylinder, a CO_2 enclosing layer provides the electrical insulation to the rest of the detector. [24]

3.2.3 Time Of Flight Chamber (TOF)

The **T**ime **O**f **F**light detector covers the TPC and is responsible for the identification of particles with intermediate momentum (up to 2.5GeV/c for Pions and Kaons, 4.0 GeV/c for Protons). Its seperation capabilities between Kaon and Proton as well as Pion and Kaon are better than 3σ. Like the TPC it covers a pseudo-rapidity range of $|\eta| < 0.9$ and the full azimuthal angle. Its polar acceptance is between $45°$ and $135°$. With its inner radius of 370cm and an outer one of 399cm it is responsible for 30% of the total material budged of the ALICE detector. The modular structure with 18 sectors contain 5 detector modules each. These modules in turn contain 15 or 19 strips of Multi-gap Resistive-Plate Chambers (MRPC), depending on their position (15 in the central and 19 in the other ones). The principle of these detectors is a

high electric field and a gaseous volume between to resistive plates, which causes traversing particles to create an electron avalanche. The MRPCs have multiple of these gaps (2x5, since it is a double MRPC design). This design allows the fast readout and high time resulltion necessary for the high multiplicities archived at the ALICE experiment. In combination with the timing information a precise time of flight measurement is made possible. [25]

3.3 Track reconstruction

In each of the above mentioned detector subsystems the reconstructed adjacent space time points are combined to so called clusters. Using only the information of the ITS' SPD the primary vertex is determined. Then the clusters in the TPC are fitted to tracks based on a Kalman filter from the most outer part to the inside. This track finding is performed with a constrain to the primary vertex and the tracks are saved as TPC-only tracks. The fitting continues inwards and includes information from the ITS and then outwards including the TOF detector. Then the tracks are refitted to so called global tracks, which are used to redetermine the position of the primary vertex [26]. Each global track gets assigned a track ID. This number is unique for each track in an event and provides a easy way to check for example for auto correlations, as will be done in section 4.4.

3.4 Data Analysis software

After this basic analysis the data is stored and available for further analysis by ALICE's offline framework AliRoot [27]. It is based on the data analysis framework ROOT, developed at CERN, which itself is written in C++. The raw data is organized according to the LHC data taking period and on a smaller scale in the accelerator's runs. A list of the analyzed runs to be used can be found in the beginning of e.g. [28]. Ultimately, the data is stored in Analysis Object Data (AOD), which contain all the necessary information to perform an analysis. For femtoscopic analysis so called NanoAODs are used, which contain only the bare minimum of information necessary for this kind of analysis and thus are more lightweight.

   The central part in terms of analysis in this work will be the Ntuple. This Root class is at its core an elaborate list, which can store information about events and particles very efficiently. It can store for each event the information about involved particles of interest (e.g. their reconstructed momenta and charge) or information of the event itself (e.g. position of the primary vertex and the multiparty) [29]. As will be described in section 4.1, the NanoAODs will be used an input to an event selection, which will extract the necessary information for the rest of the analysis and save it in an Ntuple.

3.5 Monte Carlo Dataset

It is possible to use Monte Carlo simulated from different event generators. They simulate collision events by generating kinematic and particle identification quantities as an output.

This can than be filtered through the simulated detector using for example GEANT3 or GEANT4, where the energy loss in the detector is simulated in so called hits. AliRoot simulates then the signal formation and processing and gives it as output in so called digits. These can be then used analogously to the detector output, meaning they can be passed to the event selection, like NanoAODs from raw data [30]. The generated information is still accessible allowing this way for example to check the analysis algorithms for efficiency. For this work the output of the event generator Pythia [31] for high multiplicity events of pp collisions at $\sqrt{s} = 13\text{TeV}$ was used, in order to recreate the actual data set as good as possible.

4 Data Analysis and Results

The data analysis is performed in two steps. First, the suitable events are selected (see section 4.1) and along with them suitable Λ and the Ξ^- candidates which pass the criteria specified in section 4.2 and 4.3, respectively. Their kinematic quantities are written into an Ntuple, allowing the second part of the analysis to be performed locally: The track cleaning, which removes further fake candidates from the sample (more details in the respective section after the general particle selection), the pair cleaning, which mainly removes auto correlations (more on that on section 4.4) and finally the calculation of the correlation function. The local analysis provides the flexibility to quickly rerun and test different analysis approaches, but reflects a downside expected for this analysis: Strange quarks are heavier than up and down quarks and thus require more energy to be produced. The Λ hyperon contains one and the Ξ^- even two and so their production yield will be lower, leading to lower statistics compared to e.g. the p-Λ or p-Ξ^- analysis, where only one hyperon was present [9]. The baryon-baryon interaction is assumed to be the same as in the case of antibaryon-antibaryon and therefore in the analysis they are treated simultaneously. In the notation the charge conjugates will be implicitly considered by the definition Λ-$\Xi^- \equiv \Lambda$-$\Xi^- \oplus \overline{\Lambda}$-$\overline{\Xi}^+$. In total, after the event and general particle selection, 8866751 events are written into the Ntuple (compared to about 10^9 events, which were available before the selection). The multiplicities of these candidates, in other words the number of candidates per event, are plotted in figure 4.1. The Reason for the about 25 thousand events, where no Ξ^- is present, are because they where identified as Ω^- hyperons and removed from the analysis (more on that in section 4.3).

4.1 Event selection

In order to extract the suitable events for this analysis, the recommended selection criteria for Run2 were applied. Firstly, only events which were collected by the high multiplicity trigger kHighMultV0 were used. An increased production of strange quark containing particles was observed in events with high multiplicities compared to those with low multiplicities [32]. The two reconstruction methods of the primary vertex (only SPD information and global tracks, as described in section 3.3) should not differ more than 0.5 cm in z direction while simultaneously having sufficient contributing tracks in the reconstructions. Further, its resolution should be better than 0.25cm. Finally, so called in-bunch pile-up events, where there is more than one inelastic pp collision per bunch crossing, are rejected. A summary of those selection criteria can be found in table 4.1.
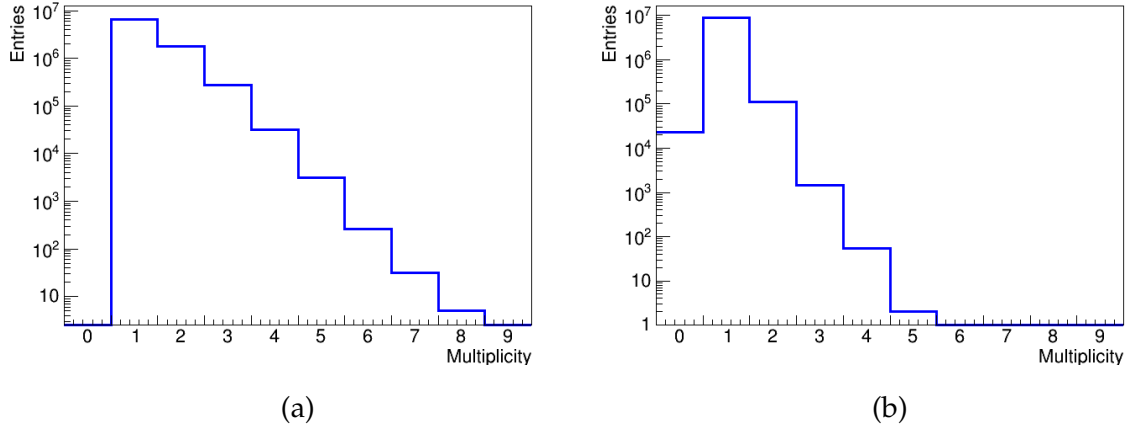
Figure 4.1: Multiplicities of the particles after their selection: In (a) the Λ and in (b) the Ξ candidates

| selection criteria	value
Trigger	kHighMultV0
z vertex	$\lvert vtx_z \rvert < 10$cm
Contributors to track vertex	$N_{contrib,track} > 1$
Contributors to SPD vertex	$N_{contrib,SPD} > 0$
Distance track and SPD vertex	$d_{vtx,track-SPD} < 0.5$cm
SPD vertex z resolution	$\sigma_{SPD,z} < 0.25$cm
Pile-up rejection	AliVEvent::IsPileUpFromSPD() AliEventUtils::IsSPDClusterVsTrackletBG()

Table 4.1: Summary of the applied event cuts

selection criteria	value
Daughter track selection criteria	
Pseudorapidity	$|\eta| < 0.8$
TPC Cluster	$n_{TPC} > 70$
Distance of closest approach	DCA > 0.05cm
Particle identification	$n_{\sigma,TPC} < 5$
Out-of-bunch pile up removal	Hit in ITS SPD or SSD or TOF timing
V_0 selection criteria	
Transverse momentum	$p_T > 0.3$GeV
Λ decay vertex	$|i_{\text{vertex}_\Lambda}| < 100cm, i = x, y, z$
Transverse radius of the decay vertex r_{xy}	$0.2 < r_{xy} < 1.5cm$
DCA of the daughter tracks at the decay vertex	DCA$_\lambda < 1.5$cm
Pointing angle α	$\cos \alpha > 0.99$
K^0 rejection	$0.48 < M_{\pi^+\pi^-} < 0.515$GeV/$c^2$
Λ selection	$|M_{p\pi} - M_{\Lambda,\text{PDG}}| < 4$MeV/$c^2$

Table 4.2: Selection criteria lambda

4.2 Λ candidate selection

The Λs cannot be directly detected by ALICE. Instead, their weak decay $\Lambda \rightarrow \pi^- + p^+$ (branching ration: 63.9%, characteristic decay length: 7.3 cm [4]) is employed, since the two daughter particles can be detected very efficiently by the ALICE detector. Tracks with opposite charges are combined after their reconstruction and before creating the AODs to a so called V^0 candidate. The name is derived from the zero net charge of these candidates and the V like shape the two daughters trace after their mother particle decays. Afterwards, selection criteria, tuned for Λs to pass, are applied to the daughter particles as well as to the V^0 candidates. The decay and the reconstruction is illustrated in figure 4.2, as well as the quantities relevant for the selection criteria, which will be discussed in the following.

The tracks have to be global, meaning they have to have left a hit in the ITS, TPC and TOF. For their identification only TPC information is used, to maximize efficiency. In order to filter out primary particles, a minimal distance of closest approach with respect to the primary vertex is required, which is determined by an extrapolation of the daughter tracks (see figure 4.2). In order to prevent fake pairs from so called out of bunch pile-up events, where two tracks from different bunch crossings are combined, the tracks are required to have a hit in the ITS SPD, ITS SDD or TOF in bunch timing. The criteria applied on the V^0 candidates are a minimum transverse momentum of 0.3GeV/c and a minimum cosine of the pointing angle, larger than 0.99. Their decay vertex can be defined by the distance of closest approach between the two daughter tracks, which from now on will be referred to as DCA$_\Lambda$. It is also used as a selection criteria by accepting only V^0 candidates with DCA$_\Lambda < 1.5$cm. The transverse radius of the decay vertex should lie between 0.2 and 100cm.
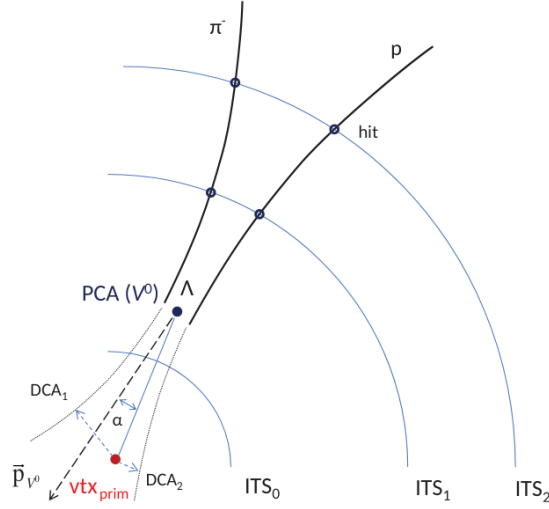
Figure 4.2: Decay and reconstruction of a V^0 [30]

Lastly, fake candidates may have been introduced via a wrong particle identification, which is particular susceptible to a K^0 contamination of the V^0 candidates when a proton passes the track selection instead of a pion and is paired with a pion with the opposite charge. In order to reject those events, the V^0 candidates' mass are calculated by assuming the masses of the daughters to be the pion masses. Particles which lie between 0.48 and 0.515 GeV/c^2 are rejected. All these selection criteria ensure a purity independent of the LHCs interaction rates and are summarized in tab 4.2.

After these selection criteria, all the survived V^0 candidates are written in the Ntuple. They will be now referred to as Λ candidates, since they passed the relevant selection criteria. Their multiplicity is, what is plotted in figure 4.1. The analysis proceeds event by event, where for all Λ candidates the four-momentum vector is calculated, by adding the four vectors of the daughters:

$$p_\Lambda = \left(\frac{E_\Lambda}{c}, \vec{p}_\Lambda \right) = \left(\frac{E_\pi}{c}, \vec{p}_\pi \right) + \left(\frac{E_\mathrm{p}}{c}, \vec{p}_\mathrm{p} \right) \tag{4.1}$$

where $\vec{p}_\pi$ and $\vec{p}_\mathrm{p}$ are the momenta measured by the ALICE detector and the energy is calculated by inserting the nominal PDG mass (see [4])

$$E_\mathrm{daughter} = \sqrt{m^2_\mathrm{PDG,daughter}/c^4 + \vec{p}^2/c^2}. \tag{4.2}$$

This has the advantage of sharpening the invariant mass distribution and reducing the propagation of systematic errors during reconstruction and identification.

Λ track cleaning

When more then one Λ are present in one event, it may happen that two (or more candidates) share the same daughter particle. Figure 4.3 illustrates this situation. The first Λ has both the
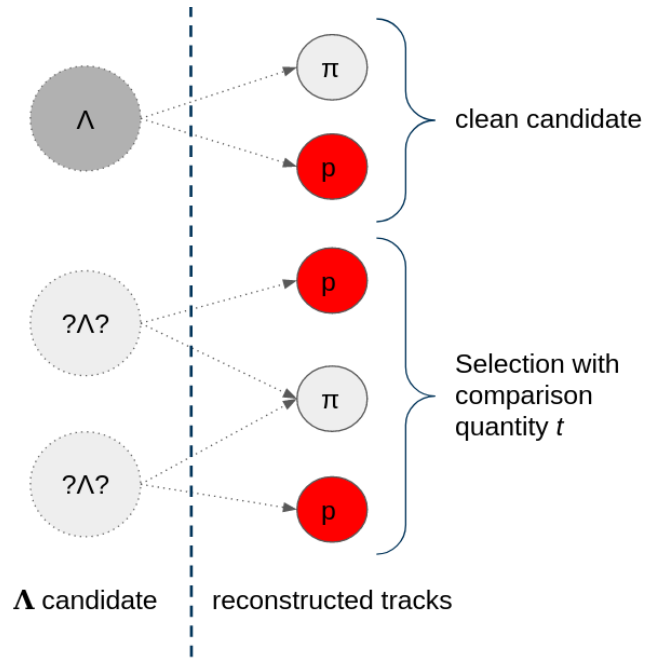
Figure 4.3: Illustration of the track sharing in the case of Λ candidates

(a) invariant Mass

(b) DCA

(c) cos(PA)
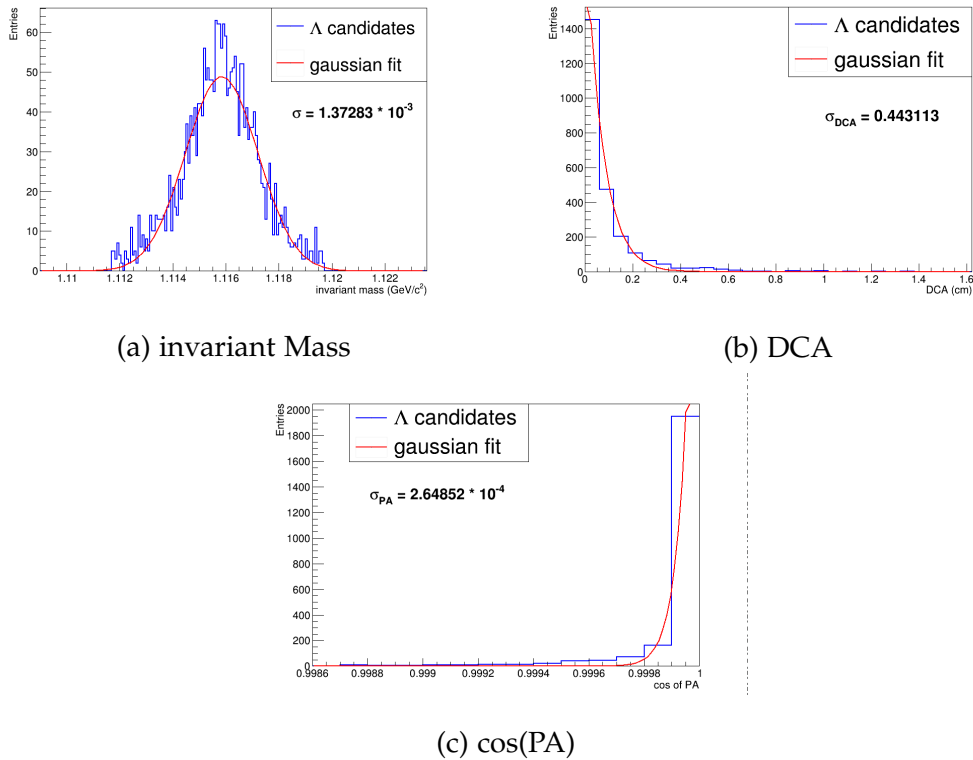
Figure 4.4: Obtainment of the weighting factors for the Λ candidate track cleaning

daughters unambiguously assigned to it. These particles make up the "clean" sample and they are assumed to be real. Corrections to that will be done with the λ parameters. The two other candidates (marked with a question mark) have an ambiguity in their reconstruction because one daughter (here the pion) is assigned to both of them. Obviously, only one of them can be a real Λ. Mostly this contamination is introduced because of the limited track resolution of the detector. It can ether not distinguish two tracks from each other when they are too close, or it registers a single track as two distinct ones (so called track splitting). A careful selection has to be performed in order to select the true candidate. It is particularly difficult because all of them have passed the selection criteria specified above. The candidates with shared daughters can be identified via the track ID, which the detector assigns to them during the reconstruction (see 3.3). In each event those candidates are separated from the clean particles and for each of them the comparison quantity t is calculated, which is defined as

$$t \equiv a_1 \cdot \left| m_{\Lambda,\text{candidate}} - m_{\Lambda,\text{PDG}} \right| + a_2 \cdot \text{DCA}_\Lambda + a_3 \cdot \left| \text{PA}_\Lambda - 1 \right|, \tag{4.3}$$

where the two quality parameters DCA_Λ and CPA_Λ from table 4.2 appear as well as the invariant mass. It is defined in such a way, that an an ideal Λ candidate would have the value $t = 0$. The Λs with the same shared track are compared with each other with respect to that value and the candidate with the smaller t is reintegrated into the sample as a "rescued" candidate. The other(s) are dumped from the sample and will not be considered in the further analysis. The weighting factors a_i in (4.3) ensure an equal contribution of all the three quality parameters. They are "trained" into (4.3) with the help of Monte Carlo simulated data, on which the above described selection were performed. For simulated particles it is known, which are true candidates and which fake. Again, the candidates with shared tracks are separated and out of those the true candidates are selected and plotted in figure 4.4. The distributions are fitted (shown in red) with a Gaussian in case of the invariant mass and with half a Gaussian in case of the DCA and the CPA. Then the parameters a_i are set to the inverse of one standard deviation of the respective fit.

It was important to find a selection that does not bias the total sample towards any of the three quality variables. Figure 4.5 shows the results of the track cleaning as it is applied on data, where the distributions of the clean (blue), rescued (green) and dumped (red) Λ candidates are shown. To be better comparable, they are normalized such that they have the same integral. Figure 4.4 (a) shows the invariant mass, which deviates only a little from a flat distribution. This has most probably to do with the large feed-down contribution of secondary Λs, where the pointing angle is bad compared to primary particles but the invariant mass is very good. The distribution of the rescued particles follows that of the clean sample, with the slight shift of the rescued curve compared to the clean one being most likely an effect of the normalization. Meaning that it could be a statistical fluctuation towards smaller invariant masses rather than a systematic bias, which gets visually amplified when normalizing to the same integral. In (b) the DCA is depicted and in (c) the cosine of the pointing angle. In both the distribution of the rescued sample initially coincides with that of the clean candidates and deviates for larger values. However, keeping in mind the

(a) invariant Mass

(b) DCA

(c) cos(PA)
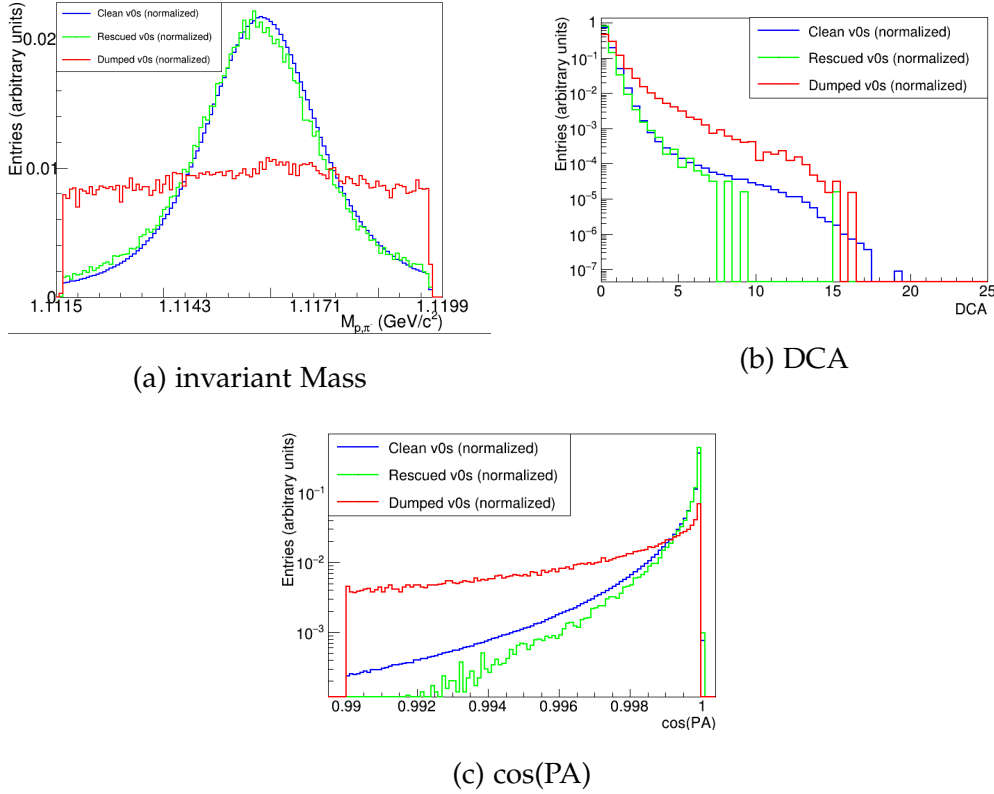
Figure 4.5: Demonstration of the track cleaning for the Λ candidates

logarithmic scale, the difference is small, especially compared to the dumped candidates. Ideally, for a bias free selection a completely flat curve would be expected but this is not possible since the criteria described in the previous section have already selected a peaked sample of particles in these two variables. In conclusion, the track cleaning seems to work as it is supposed to. It does not introduce significant biases to the sample and selects mostly the correct particles, as has been confirmed with Monte Carlo simulations. The only weak point is that this method still selects one candidate, even if all of them are fake ones, since it relies on a comparison. These are considered by obtaining the purity of the Λ candidates, as will be described in section 4.7. The track cleaning modifies the multiplicity of the Λ candidates, as can be seen in figure 4.6, where the multiplicities before and after the pair cleaning are compared to each other.

4.3 Ξ^- candidates selection

Like in the case of Λ candidates, the Ξ^- candidates are also identified via their weak decay into three charged particles $\Xi^- \rightarrow \Lambda + \pi^-$ where the Λ decays into a proton and a pion as discussed in the previous section. The branching ratio is 99.9% and the characteristic
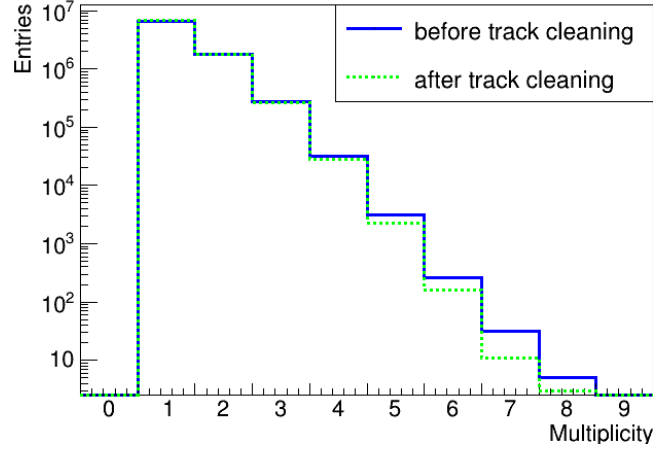
Figure 4.6: The multiplicities of the Λ candidates before and after the track cleaning

selection criteria	value
Daughter track selection criteria	
Pseudorapidity	$|\eta| < 0.8$
TPC Cluster	$n_{TPC} > 70$
Distance of closest approach	$\text{DCA}_{\text{bachelor}} > 0.05\text{cm}$
Distance of closest approach	$\text{DCA}_{\text{v0Daughters}} > 0.05\text{cm}$
Particle identification	$n_{\sigma,TPC} < 4$
Λ selection criteria	
Transverse momentum	$p_T > 0.3\text{GeV}$
Λ Pointing angle α	$\cos\alpha > 0.97$
Transverse radius of the Λ decay vertex r_{xy}	$1.4 < r_{xy} < 200cm$
DCA of the daughter tracks at the Λ decay vertex r_{xy}	$\text{DCA}(|p,\pi,\pi|) < 1.6\text{cm}$
DCA of the Λ to the primary vertex	$\text{DCA} > 0.07cm$
Λ selection	$|M_{p\pi} - M_{\Lambda,\text{PDG}}| < 6\text{MeV}/c^2$
Ξ selection criteria	
Ξ Pointing angle α	$\cos\alpha > 0.98$
Transverse radius of the Ξ dacay vertex	$0.8 < r_{xy} < 1.6\text{cm}$
DCA of the daughter tracks at the Ξ decay vertex r_{xy}	$\text{DCA}(|p,\pi,\pi|) < 1.6\text{cm}$
Ω rejection	$1.667 < \text{M}_{p,K,\pi^-} < 1.677\text{GeV}/c^2$
Ξ selection	$|\text{M}_{p,\pi,\pi} - \text{M}_{\Xi,\text{PDG}}| < 5\text{MeV}/c^2$

Table 4.3: Ξ^- candidate selection criteria

decay length 4.9 cm [4]. Analogously to the Λ selection, the tracks are combined as follows: At fist, two of them form a V^0 candidate (the daughter Λ) which then is combined with a third track (the so called bachelor) to a cascade candidate (named after the cascade of three daughters, which it produces in the detector). Selection criteria are applied to the tracks, the V^0 candidates and the cascades themselves. While staying the same for the tracks, the V^0 criteria are relaxed compared to the Λ selection (table 4.2) and DCA cuts are additionally applied with respect to the primary and the Λ decay vertex. Ideally, the V^0 candidates from the Λ reconstruction should not be reused for the Ξ^- reconstruction or viceversa. But because of the independent reconstruction of the two candidates, this may still occur. The track cleaning in the Ξ^- candidates and the pair cleaning (section 4.4) counteracts this effect. Finally, the cascade candidates also undergo the same criteria as the V^0 candidates in the Λ selection but with adjusted values. A contamination of Ω^- hyperons may be present due to a misidentified K^- as a π^-, since they decay similarly via $\Omega^- \rightarrow \Lambda + K^-$. Therefore, the invariant mass is calculated assuming a K^- as a daughter and candidates which lie around $5\,\mathrm{MeV}/c^2$ around the PDG value of the Ω's mass are removed from the sample. The selection criteria are summarized in table 4.3. The Ξ candidates are written in the Ntuple before the removal of the Ω^-s, which leads to about 25 thousand events being without a Ξ^- as can be seen in the plot of the Ξ candidate multiplicity, which is shown in figure 4.1 (b). Analogously to the Λ candidates, the four momentum vector is calculated for every candidate in order to extract from there the cinematic variables. Here, the nominal mass of the daughter Λ and the bachelor track is imposed:

$$p_{\Xi} = \left(\frac{E_{\Xi}}{c}, \vec{p}_{\Xi}\right) = \left(\frac{E_{\Lambda}}{c}, \vec{p}_{\Lambda}\right) + \left(\frac{E_{\pi}}{c}, \vec{p}_{\pi}\right) \tag{4.4}$$

where E_{π} is calculated according to equation (4.2), $\vec{p}_{\Xi}$ is calculated by adding the measured three-momenta of the two Λ daughters and finally the 0th component of the daughter Λ is calculated by

$$E_{\Lambda} = \sqrt{m_{\mathrm{PDG},\Lambda}^2/c^4 + (\vec{p}_{\Lambda,\mathrm{Daughter1}} + \vec{p}_{\Lambda,\mathrm{Daughter2}})^2/c^2}. \tag{4.5}$$
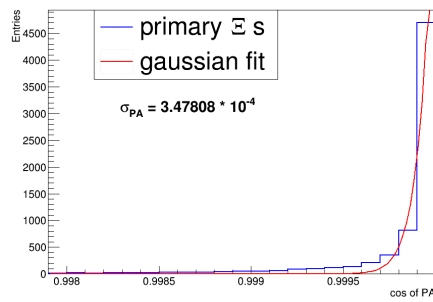
Ξ track cleaning

An analogous track cleaning as in the case of the Λ candidates has to be performed also for Ξ^- candidates. Again, the same quantity *t* like in equation (4.3) is used for the selection. The plots for the acquisition of the weighting factors, obtained in the same way as in the case of Λs, are shown in figure 4.7 together with the respective fits in red. However, more intermediate steps are necessary, because it is more likely, that a fake pair is formed out of a Λ or a bachelor pion from an already existing Ξ^-. Therefore, at first only Ξ^-s which have both Λ tracks in common are compared with each other. Then, the surviving Ξ^- candidates are checked for a shared bachelor against all other candidates in the event and selected accordingly. Finally, all other track sharing combinations are checked. Important to note is that if a Ξ^- candidate is dumped in one of the preceding steps, it will not be used for further comparison. The last step proved to be the most reliable method in the exclusion of fake
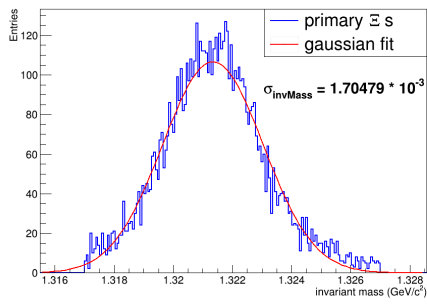
(a) invariant Mass
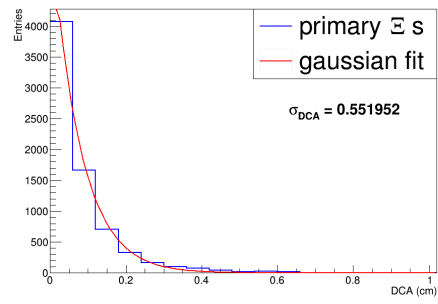
(b) DCA

(c) cos(PA)

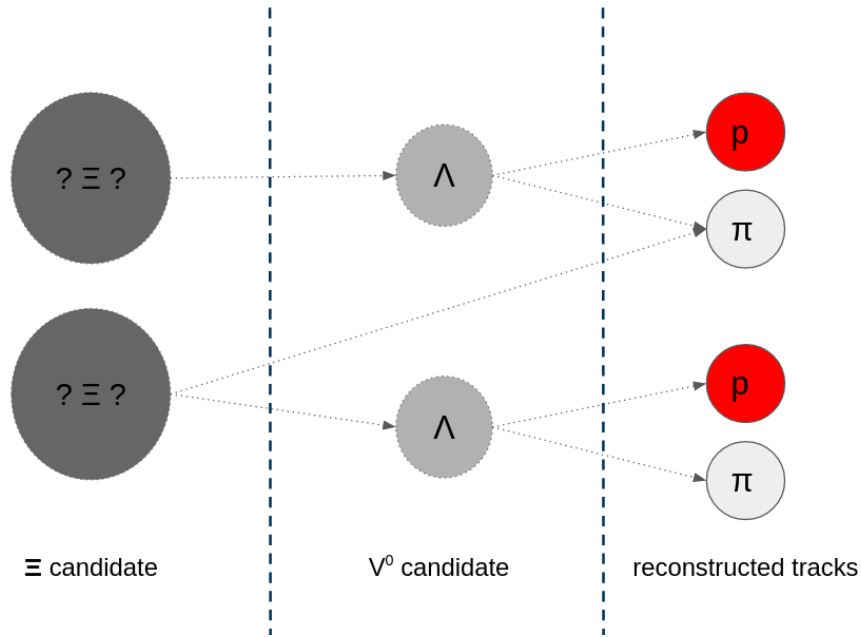Figure 4.7: Obtainment of the weighting factors for the Ξ candidate track cleaning

Figure 4.8: Example of a interwoven track sharing for the Ξs. The implemented track cleaning is efficient also in those cases

Ξ$^-$ candidates, especially when interwoven fake candidates are present, like the example in figure 4.8. Also here, this method seems to be efficient and not biasing the rescued sample in any of the three variables. The results are demonstrated in figure 4.9 in the same manner as in section 4.2. Notable is the fact that the invariant mass distribution of the dumped candidates is completely flat and that the cos(PA) of the clean and the rescued sample coincide in a larger range compared to the Λ candidates, while the DCA is comparable. This further confirms that the effects witnessed in the respective results for the Λ track cleaning are in fact due to the feed-down contributions of secondary candidates, since they are more dominant in the case of Λ than in the case of Ξ$^-$. The modified multiplicities of the Ξ$^-$ candidates are shown in figure 4.10 where they are also compared to the multiplicities before the track cleaning.

4.4 Pairing

The particles that survived the track cleaning can now form pairs, for which the relative momentum k^* is going to be calculated. Attention has to be made as to not pair a daughter Λ with its mother Ξ$^-$. These so-called auto correlations deform artificially and drastically the correlation function and overshadow the effects of the femtoscopic contributions. They can be tackled with the help of the track IDs. Thus, before pairing, all the tracks of the each particle are compared and if any of the daughters are shared, the pairing is blocked. This step will be referred to as the pair cleaning.

The question that arises is what should be done with the particles, if their pair is blocked.

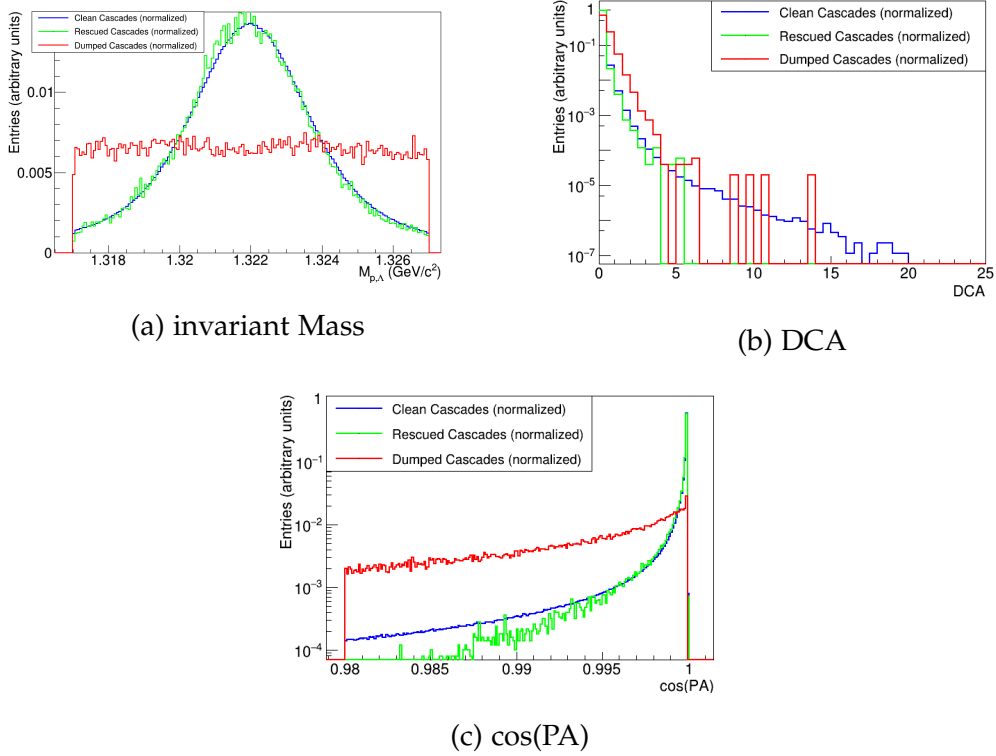(a) invariant Mass

(b) DCA

(c) cos(PA)

Figure 4.9: Demonstration of the track cleaning for the Ξ^- candidates
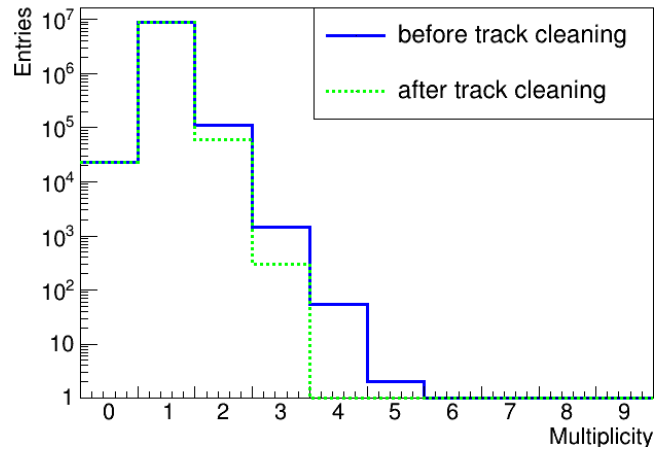
Figure 4.10: The multiplicities of the Ξ^- candidates before and after the track cleaning

Pairs before the pair cleaning

Cascade Origin	primary	weak	material	fake
fake	63197	28751	1508	24332
material	253	2437	2	69
weak	176	3456		26
primary	73579	1.42407e+06	357	8712

v0 Origin

(a)

Pairs after the pair cleaning (allowing daughter Λ)

Cascade Origin	primary	weak	material	fake
fake	6797	1128	34	573
material	253	49	2	29
weak	176	30		19
primary	73579	11979	357	5492

v0 Origin

(b)

Pairs after the pair cleaning (banning daughter Λ)

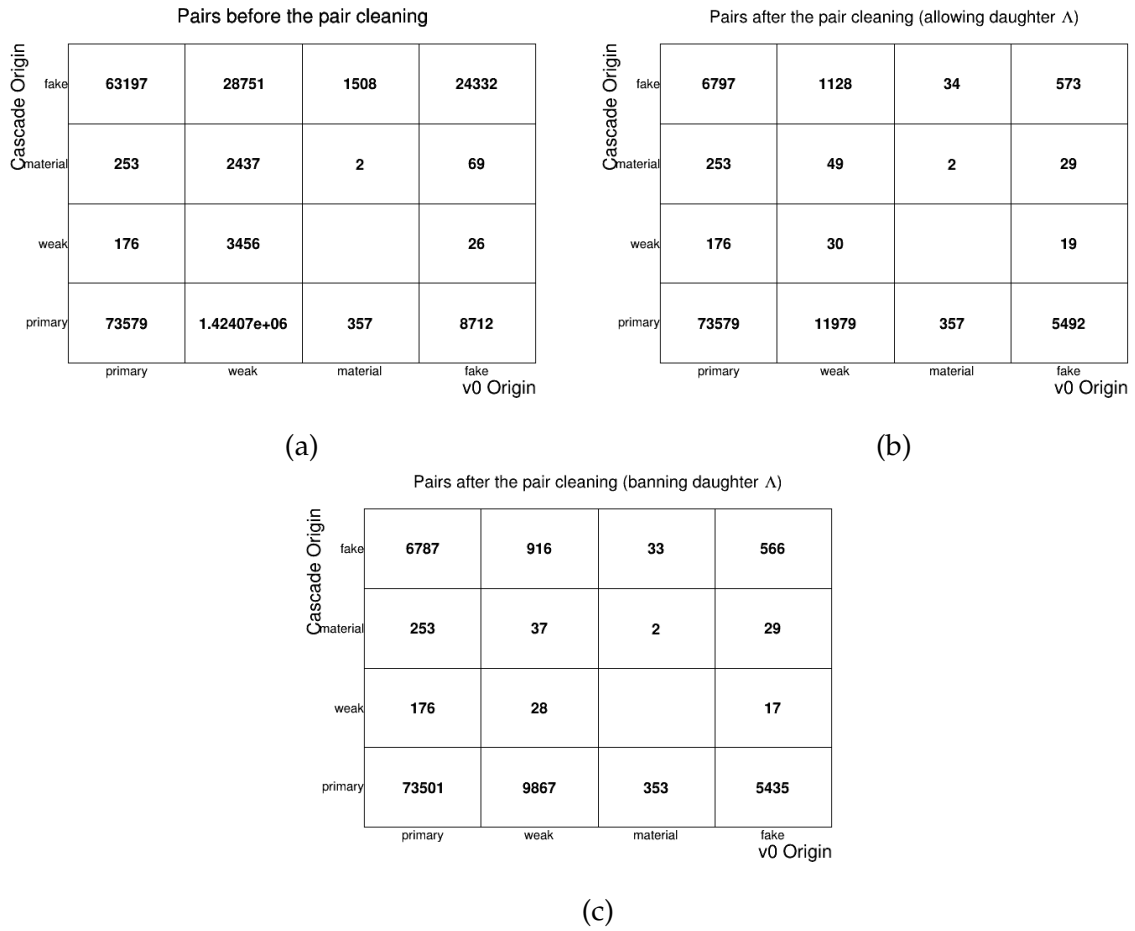| Cascade Origin	primary	weak	material	fake
fake	6787	916	33	566
material	253	37	2	29
weak	176	28		17
primary	73501	9867	353	5435

v0 Origin

(c)

Figure 4.11: Origin of the pairs from Monte Carlo simulation: In (a) before the pair cleaning, in (b) after the pair cleaning and in (c) as a comparison the result of banning daughter Λs completely

It is assumed, that the Λ is a daughter of the Ξ^- because the cases where the Ξ^- is a fake candidate combined out of a Λ and a pi^- should have been eliminated by the Ξ^- track cleaning. Thus, one should for sure not ban the Ξ^-, because it could have experienced FSI with other Λs. The daughter Λ on the other hand would not, as discussed in section 2.3.1, so removing it completely from the sample decreases the contamination with wrong pairs. There is a problem to this approach, though: The fractions for the different feed-down contributions are distorted and thus the calculation of the λ parameters as described in section 2.3.1 has to be adjusted. But it is difficult to estimate how large this distortion is for the following reasons: It could be, that the Λ is a daughter of a Ξ^- that could not be reconstructed. If so, there would be no way of identifying it as a weak daughter. This happens especially for low transverse momenta. Or it could be a daughter of another not reconstructed particle e.g a Σ^0 (details to the different feed-down contributions will be discussed in section 4.7). Although it would be in principal possible to try and reconstruct all the other hypothetical mother particles, it would introduce further uncertainties additional to not being reconstructed with a hundred percent efficiency, especially for larger transverse momenta.

Therefore, for this analysis the decision has been made, to prevent only the pairing of a Ξ^- with its own daughter Λ but allow both of them to be paired with every other candidates from the other species in the same event. Of course this approach has to be justified by its impact on the correlation function. A short discussion on this will be dedicated in section 4.6.

Additional justification can be obtained by consulting Monte Carlo simulated data. The particles are categorized with respect to their origin: "Primary" particles come directly from the emitting source, shortly decaying resonances or other primaries with such small life times, that they are indistinguishable from other primaries (for example the Σ^0 decay into Λ; more on that in section 4.7). "Weak" particles are the feed-down contribution from the weak decays of primaries. "Material" come from interactions with the detector or instrumental material and "fake" candidates are formed by misidentified daughters or are combinatorial background. In the λ parameters, the last two categories considered together as fake contributions. Figure 4.11 (a) shows all the possible pairs before the pair cleaning is performed while (b) depicts the situation after the pair cleaning. While the primary Ξ^- - weak λ contribution dominates the pair compositions due to the numerous auto-correlations, it is reduced by two orders or magnitude and is now only the second largest contribution. As a comparison, the same plot is shown in figure 4.11 (c) for the case where the identified daughters are banned completely from the analysis. The reduction of the contribution of weak pairs is rather low. Attention is necessary, when interpreting these plots: They are only differentiated according to their origin, which means, that the primary-primary pairs are not necessarily all a Λ-Ξ^- pair. The total number of possible true Λ-Ξ^- pairs in this MC sample is 73855. After the pair cleaning, where the Λ daughters are not completely banned, there are still 72226 of them left. As a comparison, when the daughter Λ are completely excluded, the number of true pairs is 72207. This reduction is because of the cases, where the assumption from above is not valid and the Λ is a primary one. It is evidently only a small effect, but together with the only small reduction of the weak Λ contribution it justifies the method of keeping the identified Λs in the analysis in order to not rig the fractions for the λ parameters.
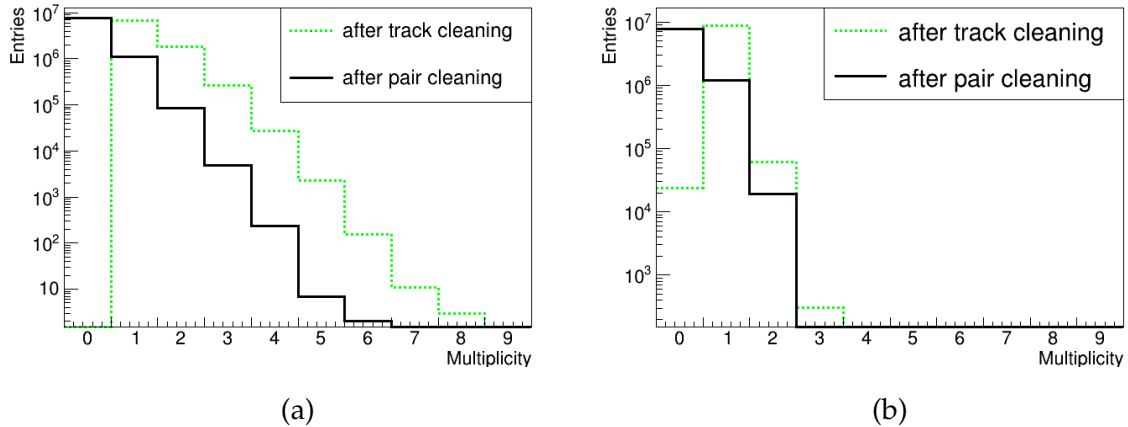
(a)   (b)

Figure 4.12: Multiplicities of the particles after the pairing: In (a) the Λ and in (b) the Ξ^- candidates

k^* range	Number of pairs
$0 < k^* < 200\text{MeV}/c$	6140
$0 < k^* < 6\text{GeV}/c$	1306137

Table 4.4: Number of $\Lambda\Xi^-$ pairs in the correlation function

With all that selections applied, the multiplicities of the Λ and Ξ candidates, which are ultimately considered in the correlation function, are depicted in figure 4.12 (a) and (b) respectively and compared to those after the track cleaning in order to demonstrate the impact of the pair cleaning also in this regard. The numbers of pairs are summarized in table 4.4 for the whole k^* range and for pairs with $k^* < 200\text{MeV}/c$. The k^* distribution of these pairs is shown in figure 4.13 up the $k^* = 5\text{GeV}/c$.

4.5 Mixing

Now only the mixed event distribution (ME), i.e. the denominator of equation 2.6 is missing. For that, the particles that participate in the pairing have to be mixed so that they are then again paired with particles from different events. This way a k^* distribution of uncorrelated pairs is build out of particles which where filtered through the particle selection and the track cleaning. The particles should not mixed completely randomly but rather with the condition of having similar experimental event properties in order to avoid effects of different detector acceptances. This is archived by saving the Λ and Ξ candidates after the pairing for the same event distribution along with their event multiplicity and the z position of the primary vertex in so called mixing boxes (realized with the C++ std::vector class). Every time a new event is analyzed and before adding the new candidates to the mixing boxes, they are paired with all already existing candidates which are similar in both of these two quantities. The resolution
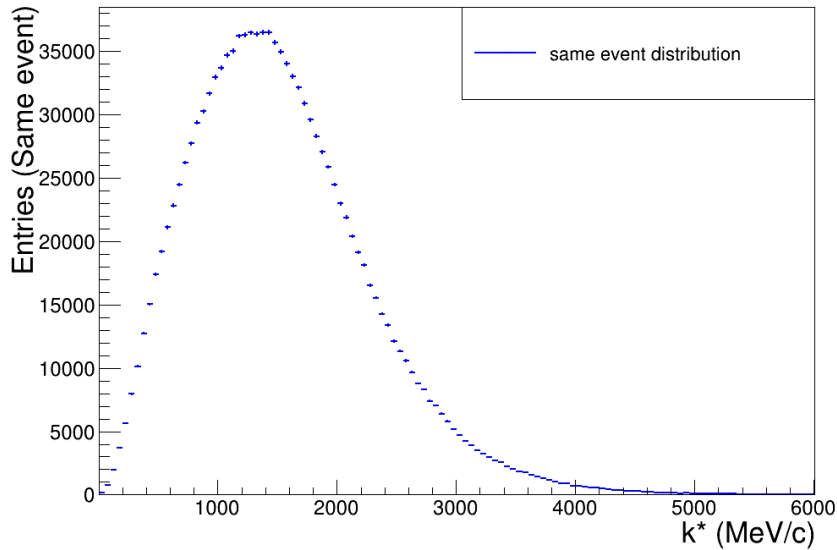
Figure 4.13: The same event distribution (SE)

of these boxes can be seen in the binning of figure 4.15 (a) for the multiplicity, where it is plotted for all considered mixed pairs. It has 25 bins for the Multiplicity range 0-100 (meaning four per bin) and a last 25th bin that contains everything above. For the vertex *z* position a bin width of 1cm is chosen, resulting in a total of 10 bins, since one of the event selection criteria was $|z_{vtx}| < 10$cm (see table 4.1. The performances of the LHC and ALICE vary over time, so in order to avoid artificial effects also from here, the mixing boxes are emptied about every 100 runs. The resulting ME distribution is shown in figure 4.14. It was normalized and reweighed as will be described in the next section.

4.6 Experimental Correlation function

Before dividing the two k^* distributions according to 2.6 a correction has to be made because of the difference in the multiplicity distributions of the same and mixed event distributions. This difference leads to a different statistical weight of the k^* distributions and deforms artificially the correlation function. Therefore, the ME has to be reweighed in such a way, that the multiplicity distribution of the ME matches that of the SE. The difference in this analysis is small, as it is shown in figure 4.15 (a), where the pair multiplicity before (dotted line) and after (continuous line) the re-weighting is depicted. That means, that influence on the mixed event k^* distribution is also small as figure 4.15 (b) shows, where the ratio of the ME before with the ME after re-weighting is plotted. The difference stays below the level of 1.5% and is most notably for very large values of k^*.

Finally, the experimental correlation function can be calculated. The result is shown in blue in figure 4.16 (a) and (b) for a smaller and a larger k^* region, both with a binning of
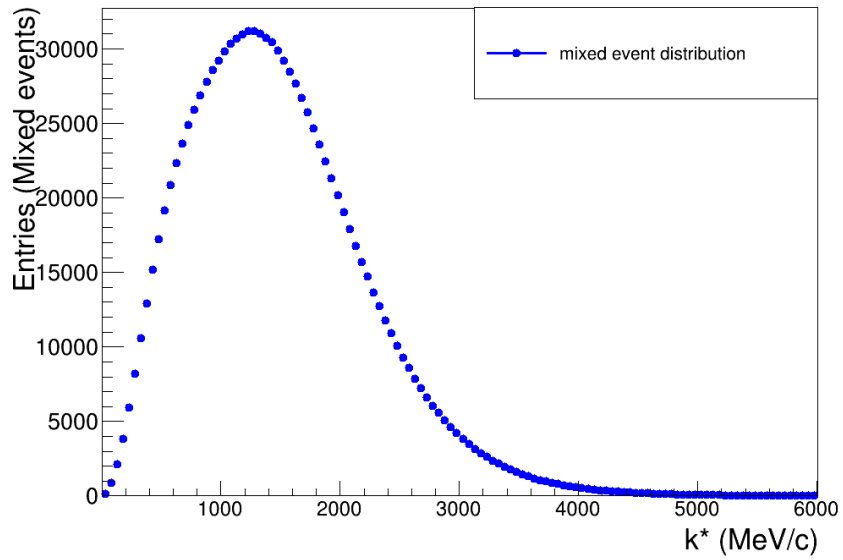
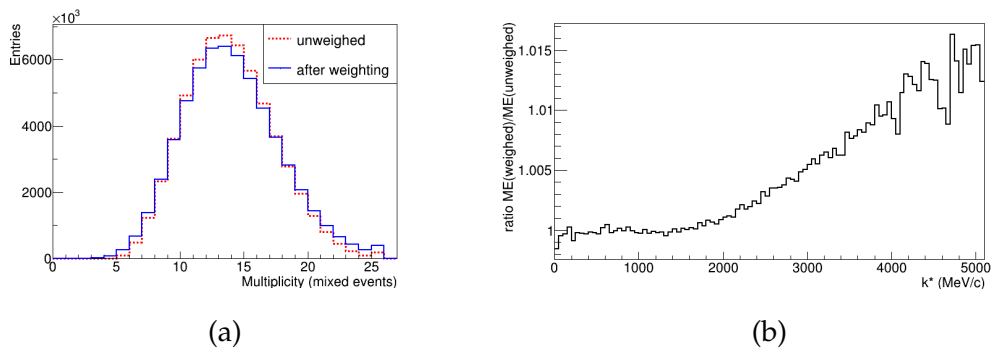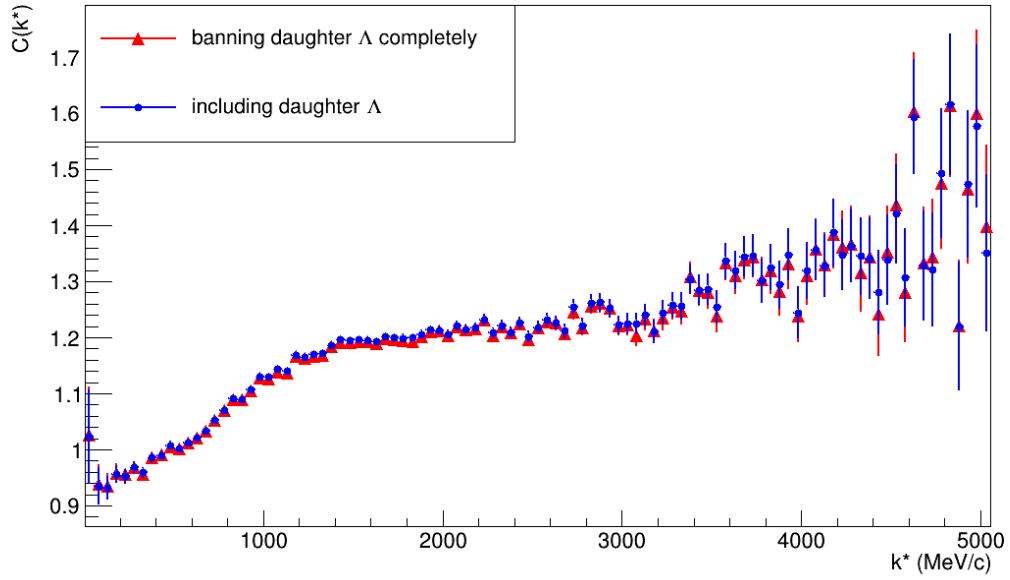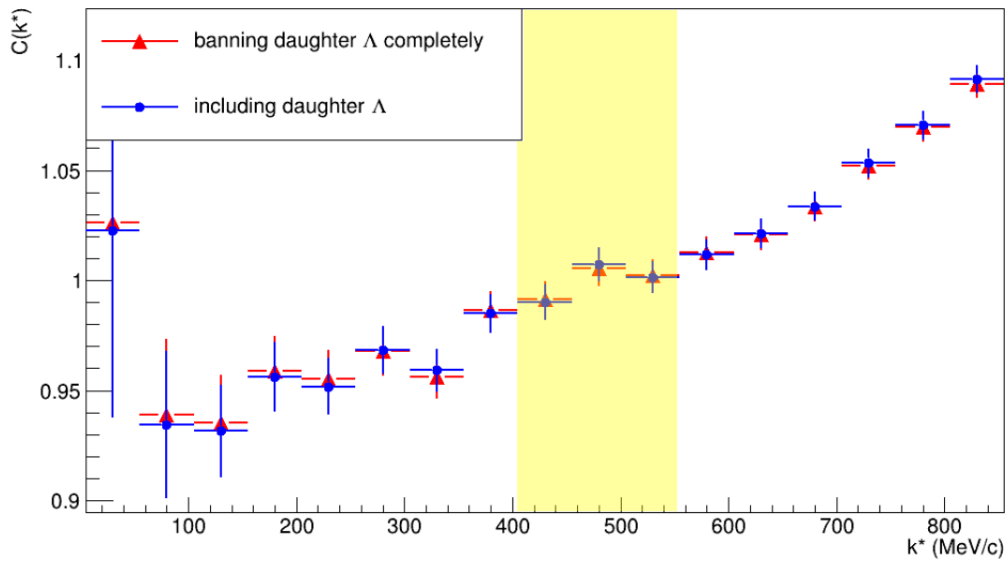Figure 4.14: The mixed event distribution (ME)

(a)

(b)

Figure 4.15: The effect of the re-weighting of the ME. (a) The pair multiplicity before and after, (b) the ratio of the ME before with the ME after the re-weighting

(a)

(b)

Figure 4.16: The experimental correlation function. The interval of normalization is high-
lighted in (b)

50MeV/c per bin. The errors are purely statistical and confirm the anticipated low statistics. The highlighted area in (a) indicates the region of normalization that was chosen, for which $C(k^*)$ should be equal to unity. It was chosen such, that it lies outside of the femtoscopic region and also outside of the non-femtoscopic background, which creates the increase for large k^*. As a comparison the red plot corresponds to the obtained correlation function, when the daughter particles are completely removed during the pair cleaning as discussed in section 4.4. The difference lies completely within the statistical uncertainties and thus the strategy of including consciously the daughter Λs is justified also experimentally.

A good check for if the selection works as intended is to build the correlation function with reconstructed and true Monte Carlo data and compare the two functions. True Monte Carlo refers here to the output of the simulation, after it has been filtered through the detector and reconstruction system. Both of them are shown in figure 4.17 (a) and in (b) their ratio for better comparison. They are in agreement within the statistical errors. The reason for their difference is that a small fraction of real pairs is wrongly excluded as well as false pairs, which passed the analysis. Figure 4.11 (b) provides an overview of the particle pairs included in the reconstructed MC correlation function. The dominating number of primaries as well as the small difference between the true and reconstructed MC correlation functions provide the confidence, that the analysis algorithm is working well.

## 4.7 Estimation of feed-down and fake candidates

Analogously to the proton-Ξ^- and proton-Λ analysis [9] the same respective contributions to the Λs and the Ξ^-s are considered, which leads to the following decomposition:

$$
\begin{aligned}
\{\Lambda\Xi^-\} =& \Lambda\Xi^- + \Lambda\Xi^-_{\Xi^-(1530)} + \Lambda\Xi^-_{\Xi^0(1530)} + \Lambda\Xi^-_{\Omega} + \Lambda\widetilde{\Xi}^- \\
&+ \Lambda_{\Xi^-}\Xi^- + \Lambda_{\Xi^-}\Xi^-_{\Xi^-(1530)} + \Lambda_{\Xi^-}\Xi^-_{\Xi^0(1530)} + \Lambda_{\Xi^-}\Xi^-_{\Omega} + \Lambda_{\Xi^-}\widetilde{\Xi}^- \\
&+ \Lambda_{\Xi^0}\Xi^- + \Lambda_{\Xi^0}\Xi^-_{\Xi^-(1530)} + \Lambda_{\Xi^0}\Xi^-_{\Xi^0(1530)} + \Lambda_{\Xi^0}\Xi^-_{\Omega} + \Lambda_{\Xi^0}\widetilde{\Xi}^- \\
&+ \Lambda_{\Sigma^0}\Xi^- + \Lambda_{\Sigma^0}\Xi^-_{\Xi^-(1530)} + \Lambda_{\Sigma^0}\Xi^-_{\Xi^0(1530)} + \Lambda_{\Sigma^0}\Xi^-_{\Omega} + \Lambda_{\Sigma^0}\widetilde{\Xi}^- \\
&+ \widetilde{\Lambda}\Xi^- + \widetilde{\Lambda}\Xi^-_{\Xi^-(1530)} + \widetilde{\Lambda}\Xi^-_{\Xi^0(1530)} + \widetilde{\Lambda}\Xi^-_{\Omega} + \widetilde{\Lambda}\widetilde{\Xi}^-
\end{aligned}
\tag{4.6}
$$

where the subscript denotes the mother particle of this feed-down contribution and the tilde refers to a misidentified particle of the respective species. The purity is calculated by plotting the invariant mass of the particles for the transverse momentum ranges (in GeV/c) $[0.3 - 0.8], [0.8 - 1.3], ..., [5.8, 6.3]$. The first range $[0 - 0.3]$ is not considered, because the reconstruction in this regime is not as efficient and contributes only a little to the total particle yield. The cut on the invariant masses of the Λ and Ξ^- candidates selection was relaxed to ±30MeV/c and ±60MeV/c respectively. The above mentioned analysis steps (track cleaning, pair cleaning etc.) were performed also on that sample and the particles that particles that contribute ultimately to the correlation function are divided in these p_T ranges. The background consists mostly of combinatorial background, which are wrongly combined
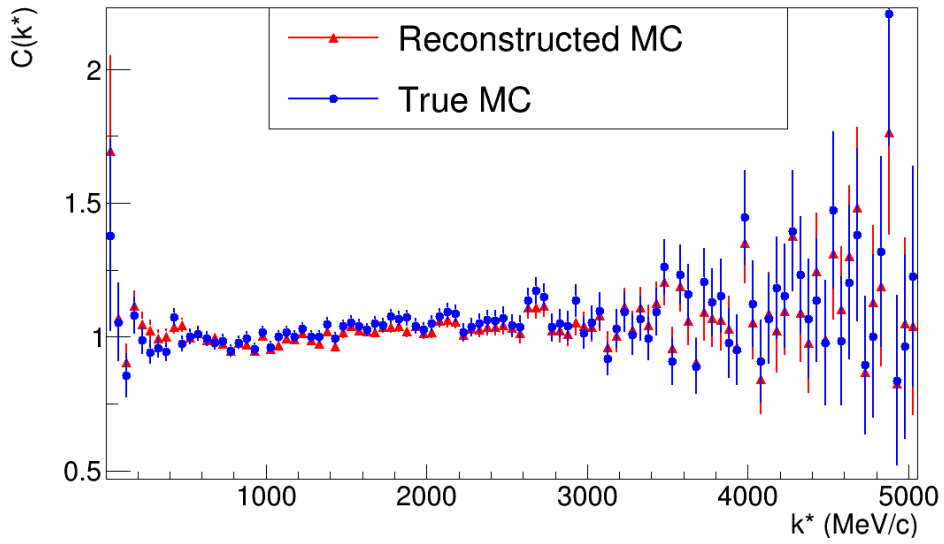
(a) true and reconstructed MC
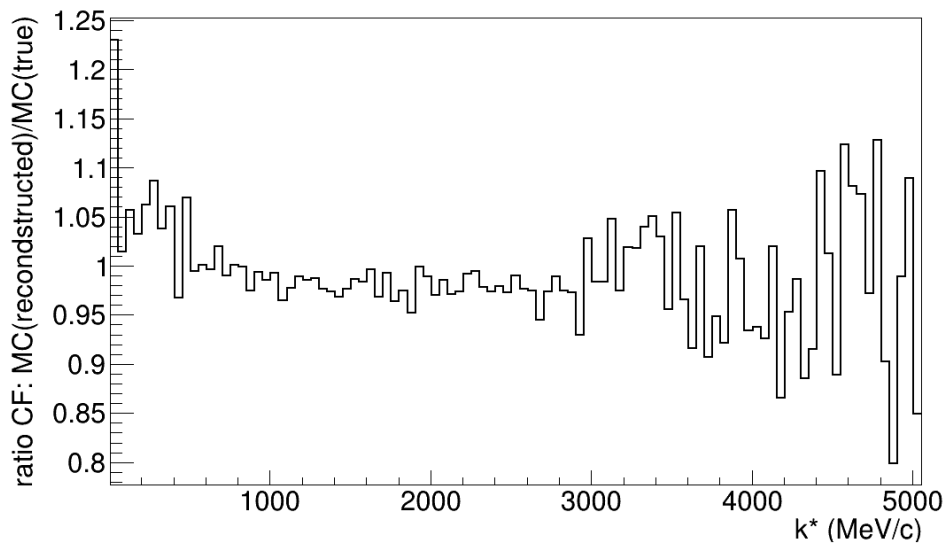
(b) the ratio between true and reconstructed MC

Figure 4.17: Correlation function with MC

Parameter [limits]	Λ	Ξ
$\Delta m (\text{GeV}/c)$	1.08	1.26
p_0	bin content at $m = 1.15\text{GeV}/c$	bin content at $m = 1.23\text{GeV}/c$
p_1	0, [open]	
p_2	$p_0 \cdot 40, [0, 200 p_0]$	
p_3	$m_{\text{PDG}} - 0.0001, [m_{\text{PDG}} \pm 0.001]$	
p_4	$0.0015, [0.001, 0.0025]$	
p_5	$p_0 \cdot 10, [0, 100 p_0]$	
p_6	$m_{\text{PDG}} + 0.0001, [m_{\text{PDG}} \pm 0.001]$	
p_7	$0.003, [0.0025, 0.005]$	
Obtained purity	95.0%	94.0%
Resolution ($2 \cdot \sigma$)	$1.5\text{MeV}/c^2$	$2.1\text{MeV}/c^2$

Table 4.5: Initialization, limits and results of the invariant mass fits

tracks. The distribution is then fitted with the following function

$$p_0 + p_1 \cdot (x - \Delta m) + p_2 \cdot \exp\left(-0.5 \cdot ((x - p_3)/p_4)^2\right) + p_5 \exp\left(-0.5 \cdot ((x - p_6)/p_7)^2\right) \quad (4.7)$$

which is essentially a Gaussian signal with a linear background. Two Gaussians are used in order to better fit the signal. The initialization parameters as well as their limits are listed in table 4.5. The purity $\mathcal{P}$ for each p_T range is defined as the ration of the Integral of the background and the sum of the integrals of the background and signal: $P(p_T) = I_{\text{Signal}}/(I_{\text{Signal}} + I_{\text{Background}})$. As resolution $2 \cdot \sigma$ is taken and it is calculated by averaging the standard deviations of the two Gaussian used for the fitting weighed with their respective integral. The integration is executed in the invariant mass window of $4\text{MeV}/c$ around the Λ's PDG mass and $5\text{MeV}/c$ around that of the Ξ^-. In order to obtain the value for the total purity and resolution, the results of each range are weighted with the number of entries in the signal region and averaged afterwards. The results are are also listed in table 4.5. The purity of the individual ranges along with the invariant mass distribution and the fit result can be found in figure 4.18 for the Λs and in figure 4.19 for the Ξ^-s, together with their respective purity and resolution.

The fractions have already been calculated in the p-Λ and p-Ξ^- analysis in [9] will be used also in this work since this analysis was also performed on high multiplicity events from pp collisions at $\sqrt{s} = 13\text{TeV}$. Slight adjustments will be done, to consider the difference in the purity. Starting with the Λs, the secondary contribution of 16% (and subsequently 84% for the primaries) is adopted from [9] while the contribution for fake and material is $1 - \mathcal{P}_\Lambda = 6\%$. From the secondaries 49% are attributed to weak Ξ^- and 48% to weak Ξ^0 decays. The last feed-down contribution is that from Σ^0, which almost exclusively decays electromagnetically to $\Lambda + \gamma$ with a mean life time $\tau = 7.4 \cdot 10^{-20}$s [4]. This timescale is too small for the detector to distinguish these Λs from the primaries and too large to have final state interactions with other primaries. So their particle yield is included in the 78% fraction for primary Λs. An
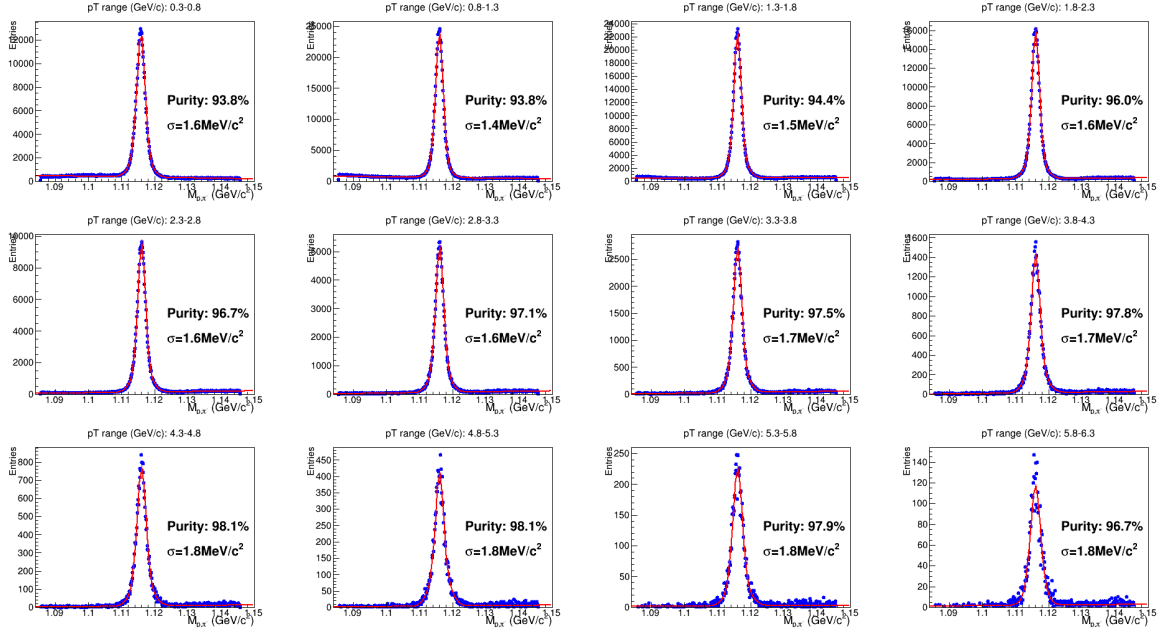
Figure 4.18: Purities for the Lambdas

estimation on the their portion out of the primaries can be given with Isospin considerations: The Λ is a singlet representation of the isospin, while the three Σ baryons ($\Sigma^\pm, \Sigma^0$) belong to a triplett. When the energies are sufficiently high, one Λ and three different Σs can be produced, which leads to the cross section ratio $R_{\Sigma^0/\Lambda} = 1/3$ [9]. But out of the Σs only the Σ^0 can decay to a Λ. Thus, when detecting a primary Λ, it is with a probability of 75% primordial and to 25% from the decay of a Σ^0.

The situation for Ξ^-s is simpler: All the three feed-down contributions which are considered are weak decays. The value of 32% for the $\Xi(1520)$ fractions is adopted form [9] and includes $\Xi^-(1530)$ and $\Xi^0(1530)$, since both are isospin partners. This number is multiplied with their respective branching ratio to Ξ^- of 1/3 and 2/3 respectively. The feed-down fraction of Ω^-s is very small and estimated by the 10 times smaller production yield of Ω^-s compared to Ξ^-s multiplied with the branching ratio to Ξ^- of 8.6%. The contribution of fake and material particles is 6% ($\approx 1 - \mathcal{P}$). The rest (67.14%) is attributed to the primary contribution.

With these values at hand, the λ parameters are calculated according to equation (2.8) and summarized in table 4.6. All the non primary contributions to the correlation function are assumed to be flat. This assumption should be valid to first order for most of the contributions, since the charge configuration does not allow for Coulomb interactions. This is different only for feed-down from Ξ^- into Λ (second row of (4.6)). However, this Ξ^--Ξ^- correlation is washed out because of the decay kinematics. The involved pion caries half of the momentum away and then k^* is evaluated after a transformation into the Λ_{Ξ^-}-Ξ^- pair's center of mass frame. This results into the correlation being small especially compared to the statistical uncertainties.
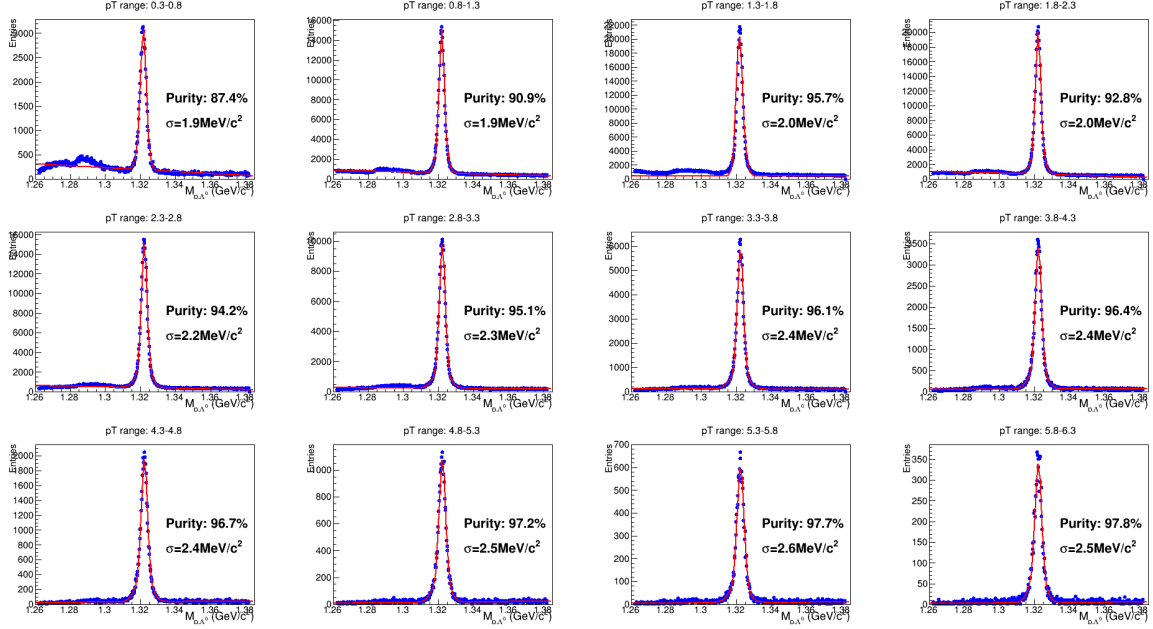
Figure 4.19: Purities for the Xis

Pair	λ [%]	Pair	λ [%]	Pair	λ [%]
$\Lambda\Xi^-$	37.9	$\Lambda_{\Xi^0}\Xi^-$	4.72	$\widetilde{\Lambda}\Xi^-$	3.11
$\Lambda\Xi^-$	6.12	$\Lambda_{\Xi^0}\Xi^-_{\Xi^-(1530)}$	0.73	$\widetilde{\Lambda}\Xi^-_{\Xi^-(1530)}$	0.48
$\Lambda\Xi^-_{\Xi^0(1530)}$	12.12	$\Lambda_{\Xi^0}\Xi^-_{\Xi^0(1530)}$	1.46	$\widetilde{\Lambda}\Xi^-_{\Xi^0(1530)}$	0.95
$\Lambda\Xi^-_\Omega$	0.6	$\Lambda_{\Xi^0}\Xi^-_\Omega$	0.06	$\widetilde{\Lambda}\Xi^-_\Omega$	0.04
$\Lambda\widetilde{\Xi}^-$	3.5	$\Lambda_{\Xi^0}\widetilde{\Xi}^-$	0.41	$\widetilde{\Lambda}\widetilde{\Xi}^-$	0.27
$\Lambda_{\Xi^-}\Xi^-$	4.82	$\Lambda_{\Sigma^0}\Xi^-$	12.71		
$\Lambda_{\Xi^-}\Xi^-_{\Xi^-(1530)}$	0.75	$\Lambda_{\Sigma^0}\Xi^-_{\Xi^-(1530)}$	2		
$\Lambda_{\Xi^-}\Xi^-_{\Xi^0(1530)}$	1.49	$\Lambda_{\Sigma^0}\Xi^-_{\Xi^0(1530)}$	4		
$\Lambda_{\Xi^-}\Xi^-_\Omega$	0.06	$\Lambda_{\Sigma^0}\Xi^-_\Omega$	0.16		
$\Lambda_{\Xi^-}\widetilde{\Xi}^-$	0.42	$\Lambda_{\Sigma^0}\widetilde{\Xi}^-$	1.12		

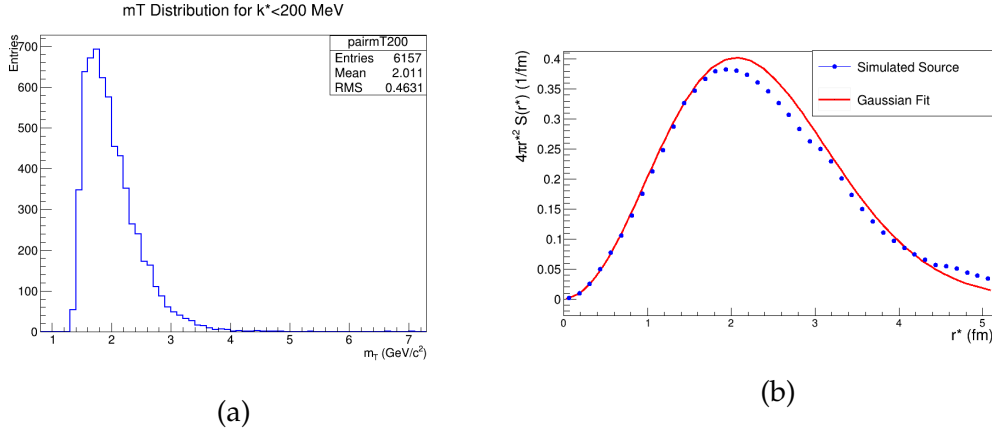Table 4.6: Results for the λ parameters

(a)

(b)

Figure 4.20: The calculation of the Source function: In (a) the m_T distribution of the particle pairs and in (b) the source function with fit

4.8 Comparison between theory and experiment

The theoretical correlation functions will be calculated with the CATS tool, using the Lednicky model. That requires a Gaussian source, specifically its radius, as input parameter. The assumption of a common core source for baryons is used to determine r_{core}. Because of the low statistics it will not be treated differentially with respect to m_T. Instead the same r_{core} is assumed for all pairs and it is determined by plotting the m_T distribution for pairs with a reduced relative momentum $k^* < 200 \text{MeV}/c$ in figure 4.20 (a). From there, the mean value is extracted ($\langle m_T \rangle = 2.011 \text{GeV}/c^2$) which, following [13] corresponds to $r_{core} = 0.8934 \text{fm}$. With that value as an input parameter CATS is able to compute the source function considering the strongly decaying resonances as described in section 2.1. They result is fitted with a simple Gaussian function in the interval 1.03-4.42fm and shown in figure 4.20 (b).

The fit should describe the in good approximation the source function for small relative distances and deviate only for larger radii. However, small deviation is observed observed in the center of the Gaussian function as well as a small deviation from the linear tail, as indicated in the most right part of figure 4.20 (b). It is unclear, whether the reason lies in an artifact of the simulation or of a physical effect, thus it has to be examined in the future. It is expected that the correction to this effect should change the obtained effective radius only slightly. The difference between the fit and the simulated source could be a normalization effect, because both distributions have to be normalized to one in order to represent a probability distribution and the deviations from the exponential tail are not considered by the Gaussian fit. The value obtained by the fit for the effective range is: $r_{eff} = 1.031 \pm 0.005 \text{fm}$.

As input for the Lednicky modell the scattering parameters and effective ranges from [33] will be used. There, the $\Lambda\Xi^-$ interaction was theoretically studied by employing chiral effective field theory (EFT) to leading order (LO). Since both particles have spin 1/2, they can couple to a singlet and triplet system. The parameters were calculated up to four different Cut Off energies, which are depicted in the first columns of table 4.7. A small systematic

	EFT				NSC97a	NSC97f	fss2
Λ (MeV)	550	600	650	700			
singlet							
f_0^0	33.5	-35.4	-12.7	-9.07	0.80	2.11	1.08
d_0^0	1.00	0.93	0.87	0.87	4.71	3.21	3.55
triplet							
f_0^1	-0.33	- 0.33	- 0.32	-0.31	-0.54	-0.33	-0.26
d_0^1	-0.36	-0.30	-0.29	-0.27	-0.47	2.79	2.15

Table 4.7: The parameters used for the theoretical computation of the correlation function with CATS. Values from [33]

variation is performed with respect to the source size: The value obtained in figure 4.20 is the mean value. Together with that, an upper limit and a lower limit have been calculated, based on the uncertainties of r_{core}. The limits are $r^*_{\text{upper limit}} = 1.094$fm and $r^*_{\text{lower limit}} = 0.971$fm. In the calculation of the theoretical correlation function a linear fit for the baseline is included. With that, the experimental data is fitted in the interval $0\text{MeV}/c < k^* < 300\text{MeV}/c$, keeping the parameters for the Lednicky model fixed and allowing only the two parameters of the linear baseline to be free. This way, the fit is performed for each of the four Cut Off values and with the three effective radii, in order to estimate the variation based on uncertainty of the source size. The results are shown in figures 4.21 - 4.24 for each Cut Off energy. Additionally the linear baseline is shown for the mean value of r^*.

The EFT calculations indicate an strong attractive potential. This can not be supported by the experimental data. They indicate rather a weak interaction, although the statistics do not provide the certainty to decide between an attractive and a repulsive interaction. Table 4.7 shows also the scattering parameters for the Nijmegen potential (NSC97a and NSC97f) and the model by Fujiwara et al. (fss2), which is also discussed in [33]. Their correlation function is compared with the experimental in figure 4.25. Unfortunately, the statistics are too large as to allow a quantitative statement on those calculations.
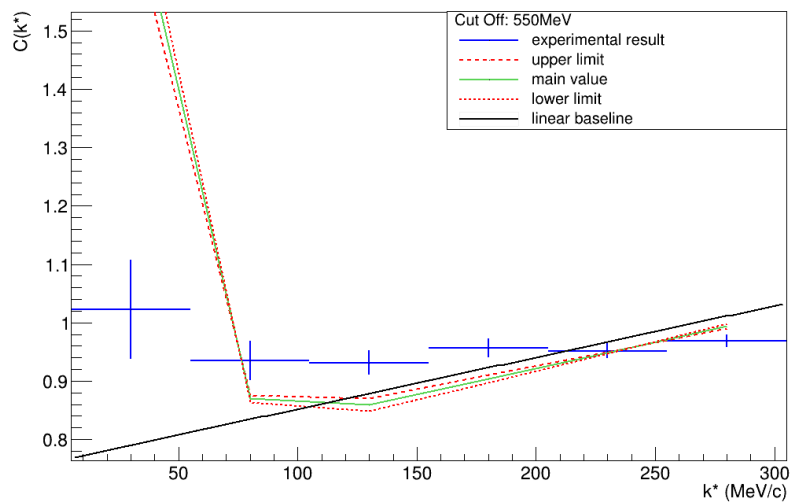
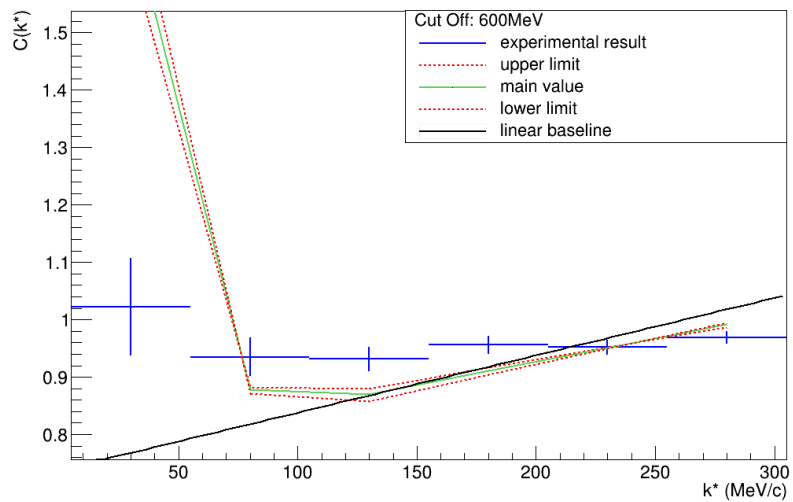Figure 4.21: Comparison with LO EFT with Cut Off at 550MeV

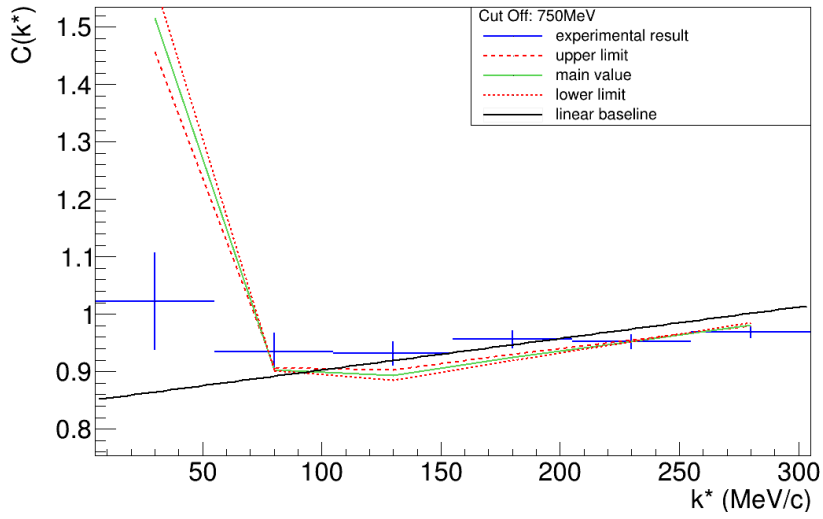Figure 4.22: Comparison with LO EFT with Cut Off at 600MeV

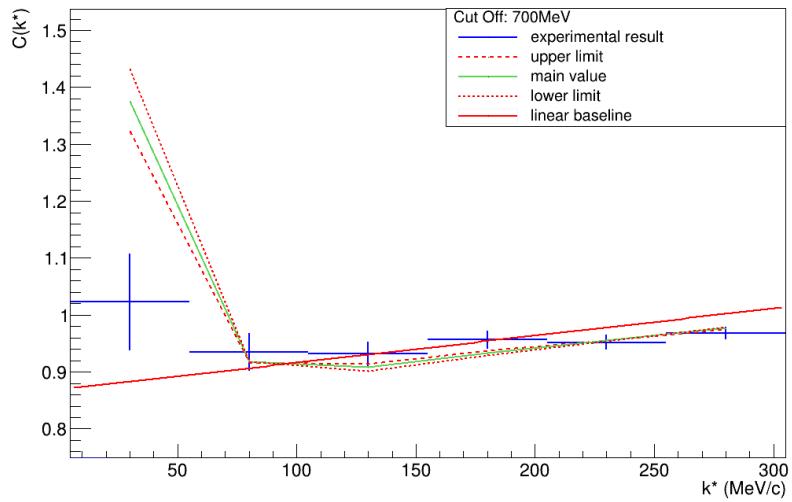Figure 4.23: Comparison with LO EFT with Cut Off at 650MeV

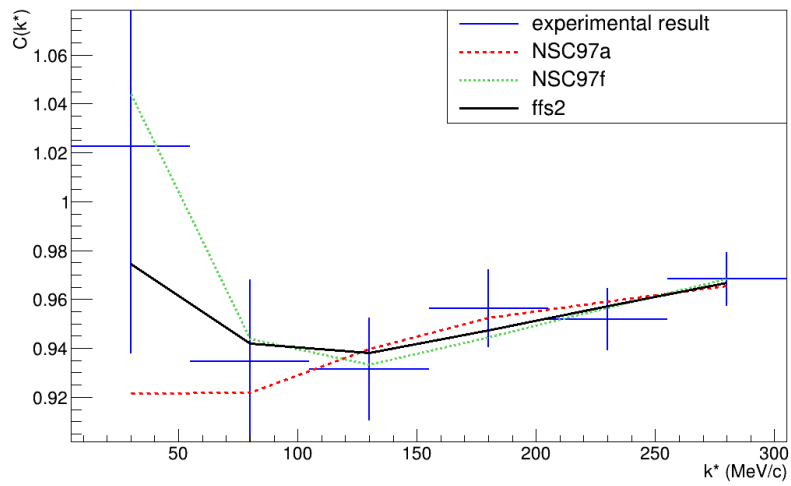Figure 4.24: Comparison with LO EFT with Cut Off at 700MeV

Figure 4.25: Comparison with the Nijmegen potential (NSC97a and NSC97f) and the model by Fujiwara et al. (fss2)

5 Summary and Outlook

Overall a robust analysis algorithm has been found to handle the analysis of Λ-Ξ^-. The analysis with Monte Carlo generated data demonstrated its effectiveness in selecting the correct particles even in the presence of fake candidates which passed initial selection criteria and exhibit good selection quality parameters. Additionally, it does so without biasing the particle sample into any of the used quality parameters. The approach used in the pair cleaning has the advantage of allowing a better calculation of the λ parameters because the fractions are not distorted to an unknown extend. This algorithm is applicable also in other systems, like p-Pb or Pb-Pb collisions. Further, it can effortlessly be applied also to other YY correlation studies, where auto-correlations are present and where a track cleaning will be necessary because of a very similar reconstruction process for all hyperons.

After the cleaning processes, the analysis was continued to the calculation of the correlation function and the comparison to theoretical models. Even with the large statistical uncertainties the experimental results were not able to reproduce the theoretical predictions made by LO EFT, indicating a rather weak interaction. This result is also applicable to the p-Ω^- analysis, where the strength of the Λ-Ξ^- is an important ingredient and was never measured before experimentally. However, the limit of the statistics was reached at the comparison with the Nijmegen potentials and the model by Fujiwara et al. as it was not possible to draw conclusions from it.

The LHC Run 3, starting in March 2021, will improve on the statistics and will hopefully allow a more quantitative study of the Λ-Ξ^- interaction. In the meantime, data from p-Pb and Pb-Pb collisions can be used, to further improve on the current statistics and to study the correlations in a system with a different source size.

Bibliography

[1]   N. Degenaar and V. F. Suleimanov. *The Physics and Astrophysics of Neutron Stars*. Springer, 2018. Chap. 5.

[2]   G. Baym, T. Hatsuda, T. Kojo, P. D. Powell, Y. Song, and T. Takatsuka. "From hadrons to quarks in neutron stars: a review". In: *Reports on Progress in Physics* 81.5 (Mar. 27, 2018), p. 056902. DOI: 10.1088/1361-6633/aaae14. URL: https://doi.org/10.1088%2F1361-6633%2Faaae14.

[3]   F. Özel and P. Freire. "Masses, Radii, and the Equation of State of Neutron Stars". In: *Annual Review of Astronomy and Astrophysics* 54.1 (2016), pp. 401–440. DOI: 10.1146/annurev-astro-081915-023322. eprint: https://doi.org/10.1146/annurev-astro-081915-023322. URL: https://doi.org/10.1146/annurev-astro-081915-023322.

[4]   M. Tanabashi, K. Hagiwara, K. Hikasa, et al. "Review of Particle Physics". In: *PHYSICAL REVIEW D* 98 (3 Aug. 17, 2018), p. 030001. DOI: 10.1103/PhysRevD.98.030001. URL: https://link.aps.org/doi/10.1103/PhysRevD.98.030001.

[5]   D. Chatterjee and I. Vidaña. "Do hyperons exist in the interior of neutron stars?" In: *THE EUROPEAN PHYSICAL JOURNAL A* (52 2016), p. 29.

[6]   P. B. Demorest, T. Pennucci, S. M. Ransom, M. S. E. Roberts, and J. W. T. Hessels. "A two-solar-mass neutron star measured using Shapiro delay". In: *Nature* 467 (), pp. 1081–1083. DOI: doi:10.1038/nature09466.

[7]   J. e. a. Antoniadis. "A Massive Pulsar in a Compact Relativistic Binary". In: *Science* 340.6131 (2013). URL: https://science.sciencemag.org/content/340/6131/1233232.

[8]   ALICE Collaboration. "A new laboratory to study hadron-hadron interactions". In: *arXiv* (2020). URL: https://inspirehep.net/literature/1797617.

[9]   A. Mathis, L. Fabbietti, B. Hohlweger, V. M. Sarti, D. Mihaylov, and O. V. Doce. "p-p, p-Λ and Λ-Λ correlations studied via femtoscopy in pp reactions at $\sqrt{s}$ = 13 TeV". In: *ALICE analysis note* (2018).

[10] R. Hanbury Brown and R. Twiss. "A Test of a new type of stellar interferometer on Sirius". In: *Nature* 178 (1956), pp. 1046–1048. DOI: 10.1038/1781046a0.

[11] U. Heinz and B. V. Jacak. "TWO-PARTICLE CORRELATIONS IN RELATIVISTIC HEAVY-ION COLLISIONS". In: *Annual Review of Nuclear and Particle Science* 49.1 (), pp. 529–579. DOI: 10.1146/annurev.nucl.49.1.529. eprint: https://doi.org/10.1146/annurev.nucl.49.1.529. URL: https://doi.org/10.1146/annurev.nucl.49.1.529.

[12] M. A. Lisa, S. Pratt, and U. W. Ron Soltz. "FEMTOSCOPY IN RELATIVISTIC HEAVY ION COLLISIONS: Two Decades of Progress". In: *Annual Review of Nuclear and Particle Science* (55 Dec. 8, 2005), pp. 357–402. URL: https://www.annualreviews.org/doi/10.1146/annurev.nucl.55.090704.151533.

[13] ALICE Collaboration. "Search for a common baryon source in high-multiplicity pp collisions atthe LHC". In: *arXiv* (Apr. 15, 2020). URL: https://alice-publications.web.cern.ch/node/6194.

[14] ALICE Collaboration. "p-p, p-Λ and Λ-Λ correlations studied via femtoscopy in pp reactions at $\sqrt{s}$ = 7 TeV". In: *Phys. Rev. C* 99.2 (2019), p. 024001. DOI: 10.1103/PhysRevC.99.024001. URL: https://journals.aps.org/prc/abstract/10.1103/PhysRevC.99.024001.

[15] R. Lednicky and V. Lyuboshits. "Final State Interaction Effect on Pairing Correlations Between Particles with Small Relative Momenta". In: *Sov. J. Nucl. Phys.* 35 (1982), p. 770. URL: https://inspirehep.net/literature/167537.

[16] D. L. Mihaylov, V. M. Sarti, O. W. Arnold, L. Fabbietti, B. Hohlweger, and A. M. Mathis. "A femtoscopic correlation analysis tool using the Schrödinger equation (CATS)". In: *The European Physical Journal C* 78 (5 Feb. 23, 2018), p. 394. DOI: 10.1140/epjc/s10052-018-5859-0.

[17] CERN. *The Higgs boson*. Ed. by cern.ch. URL: https://home.cern/science/physics/higgs-boson.

[18] J. Wenninger. *LHC Report: The final days of Run 2*. Last checked: 22.08.2020. CERN. Sept. 24, 2018. URL: https://home.cern/news/news/accelerators/lhc-report-final-days-run-2 (visited on 08/22/2020).

[19] R. Bruce. "REVIEW OF LHC RUN 2 MACHINE CONFIGURATIONS". In: (2019). URL: https://pdfs.semanticscholar.org/3be8/4c29c0d7544c2462ecb2b2b959472226e608.pdf.

[20] J. M. Jowett and M. Schaumann. "OVERVIEW OF HEAVY IONS IN LHC RUN 2". In: (2019). URL: https://www.semanticscholar.org/paper/OVERVIEW-OF-HEAVY-IONS-IN-LHC-RUN-2-Jowett-Schaumann/c383408b71b0541fff41963499e8f6ea337dd416.

[21] ALICE Collaboration. *A Large Ion Collider Experiment*. 2020. URL: https://alice.web.cern.ch/#experiment.

[22] ALICE Collaboration. "The ALICE experiment at the Cern LHC". In: *Journal of Instrumentation* 3 (2008).

[23] H. Bethe. "Zur Theorie des Durchgangs schneller Korpuskularstrahlen durch Materie". In: *Annalen der Physik* 397.3 (1930), pp. 325–400. DOI: 10.1002/andp.19303970303. eprint: https://onlinelibrary.wiley.com/doi/pdf/10.1002/andp.19303970303. URL: https://onlinelibrary.wiley.com/doi/abs/10.1002/andp.19303970303.

[24] J. A. et al. "The ALICE TPC, a large 3-dimensional tracking device with fast readout for ultra-high multiplicity events". In: *Nuclear Instruments and Methods in Physics Research Section A: Accelerators, Spectrometers, Detectors and Associated Equipment* 622.1 (Jan. 20, 2010), pp. 316–367. URL: https://www.sciencedirect.com/science/article/pii/S0168900210008910.

[25] ALICE Collaboration. "ALICE Time-Of-Flight system (TOF) : Technical Design Report". In: (2000).

[26] M. Ivanov, I. Belikov, P. Hristov, and K. Šafařík. "Track reconstruction in high density environment". In: *Nuclear Instruments and Methods in Physics Research Section A: Accelerators, Spectrometers, Detectors and Associated Equipment* 566.1 (2006). TIME 2005, pp. 70–74. ISSN: 0168-9002. DOI: https://doi.org/10.1016/j.nima.2006.05.029. URL: http://www.sciencedirect.com/science/article/pii/S0168900206008126.

[27] ALICE Collaboration. *AliRoot: ALICE Software Framework*. 2020. URL: https://github.com/alisw/AliRoot.

[28] A. Mathis, L. Fabbietti, B. Hohlweger, V. M. Sarti, D. Mihaylov, and O. V. Doce. "p-Ξ femtoscopy in pp High Multiplicity reactions at $\sqrt{s}$ = 13 TeV". In: *ALICE analysis note* (2018).

[29] R. R. Guide. *TNtuple Class Reference*. URL: https://root.cern.ch/doc/master/classTNtuple.html (visited on 10/04/2020).

[30] A. Mathis. "First Measurement of the Proton–Σ^0 Interaction via the Femtoscopy Method". PhD thesis. Technische Universität München, May 25, 2020.

[31] T. Sjöstrand, S. Mrenna, and P. Skands. "PYTHIA 6.4 physics and manual". In: *Journal of High Energy Physics* 2006.05 (May 2006), pp. 026–026. DOI: 10.1088/1126-6708/2006/05/026. URL: https://doi.org/10.1088%2F1126-6708%2F2006%2F05%2F026.

[32] J. Adam, D. Adamová, M. M. Aggarwal, et al. "Enhanced production of multi-strange hadrons in high-multiplicity proton-proton collisions". In: *Nature Physics* 13.6 (2017), pp. 535–539. ISSN: 1745-2481. URL: https://doi.org/10.1038/nphys4111.

[33] J. Haidenbauer and U.-G. Meissner. "Predictions for the strangeness S = -3 and -4 baryon-baryon interactions in chiral effective field theory". In: *Phys. Lett. B* 684 (2010), pp. 275–280. DOI: 10.1016/j.physletb.2010.01.031. arXiv: 0907.1395 [nucl-th].